ENHANCING THERMOELECTRIC POWER GENERATION EFFICIENCY WITH MOLECULAR BEAM EPITAXIAL TbAs/III-V SEMICONDUCTOR NANOCOMPOSITES

by

Laura E. Cassels

A thesis submitted to the Faculty of the University of Delaware in partial fulfillment of the requirements for the degree of Master of Materials Science and Engineering

Summer 2011

Copyright 2011 Laura E. Cassels
All Rights Reserved

ENHANCING THERMOELECTRIC POWER GENERATION EFFICIENCY WITH MOLECULAR BEAM EPITAXIAL TbAs/III-V SEMICONDUCTOR NANOCOMPOSITES

by
Laura E. Cassels

Approved: ____
Joshua M. O. Zide, Ph.D.
Professor in charge of thesis on behalf of the Advisory Committee

Approved: ____
David C. Martin, Ph.D.
Chair of the Department of Materials Science and Engineering

Approved: ____
Babatunde A. Ogunnaike, Ph.D.
Interim Dean of the College of Engineering

Approved: ____
Charles G. Riordan, Ph.D.
Vice Provost for Graduate and Professional Education

ACKNOWLEDGMENTS

I deeply thank my advisor, Dr. Joshua Zide (Jay-Z), for choosing me to be his first graduate student (and never showing his regret for that decision). He faithfully provided just the right amount of knowledge and encouragement that I needed to complete this project and survive grad school. Pretty good for a first-timer! Thank you to my fellow group members – Pernell, John, and Yujun – couldn't have picked anyone better to be locked up behind glass with for years! Thank you also to my thesis committee, Dr. Zide, Dr. Bob Opila, Dr. Ismat Shah, and Dr. Sylvain Cloutier.

Thank you to my collaborators who collected at least half of the data presented here and provided useful discussions and support: Ashok Ramu, Peter Burke, Trevor Buehl, Dr. Hong Lu, Dr. Art Gossard, Dr. Chris Palmstrøm, and Dr. John Bowers at UCSB; Tela Favaloro, Gilles Pernot, and Dr. Ali Shakouri at UCSC, and Jae Hun Seol, Dongyan Xu, Dr. Arun Majumdar, Dr. Yang Zhao, and Dr. Joe Feser (formerly) at Berkely; Chelsea Haughn and Dr. Matt Doty at UD; and Dr. Leszek Wielunski at Rutgers University. It was a pleasure working with you all.

This work was funded by DARPA and the Solar Hydrogen IGERT at the University of Delaware. Thank you to the IGERT for keeping me busy, providing me with lots of intelligent cocktail party conversation topics, and mostly thank you for all of your wonderful friendships!

Love and grrr and a million thanks to my husband John for forcing me to concentrate on writing and putting up with my consistent lack of free time! Infinite

thanks and love to mis padres for supporting me emotionally and otherwise my entire life!

TABLE OF CONTENTS

LIST OF FIGURES vii
ABSTRACT x

Chapter

1 INTRODUCTION 1

1.1 Thermoelectrics 1

1.1.1 Concepts for Thermoelectrics 1
1.1.2 Thermoelectric Devices and Applications 3
1.1.3 Thermoelectric Material Properties 5

1.2 ErAs:III-V Nanocomposites 8

1.2.1 Low-dimensional Structures in Thermoelectric Materials 8
1.2.2 ErAs Nanocomposites for Thermoelectric Power Generation 9
1.2.3 TbAs:III-V Nanocomposites 11

1.2.3.1 Properties of Rare Earth Monopnictides 12
1.2.3.2 Power Factor Enhancement with TbAs Nanoparticles 13

1.3 Overview of Thesis 16

2 EXPERIMENTAL METHODS 17

2.1 Growth of Materials by Molecular Beam Epitaxy (MBE) 17
2.2 Sample Characterization 24

2.2.1 Structural Properties 25
2.2.2 Electrical Properties 28
2.2.3 Thermal Properties 32

3 TbAs:GaAs NANOCOMPOSITES: RESULTS AND DISCUSSION 36

3.1 Characterization of TbAs:GaAs Nanocomposites 36

3.1.1 Structural Properties 37
3.1.2 Electrical and Thermal Properties 39
3.1.3 Nanoparticle Observation and Characterization 42

3.2 Summary 44

4 TbAs:InGaAs NANOCOMPOSITES: RESULTS AND DISCUSSION 45

4.1 Room Temperature Properties of TbAs:InGaAs Nanocomposites 46

4.1.1 Structure and Composition 46
4.1.2 Electrical Characterization 48
4.1.3 Thermal Characterization 52
4.1.4 Thermoelectric Performance 52

4.2 High Temperature Thermoelectric Properties of TbAs:InGaAs 53

4.2.1 Electrical Characterization 53
4.2.2 Thermal Characterization 59

4.3 Summary 63

5 CONCLUSIONS AND FUTURE WORK 65

REFERENCES 69

Appendix

REPRINT PERMISSION LETTERS 73

LIST OF FIGURES

Figure 1.1: In a conductor under a thermal gradient, charge carriers (electrons in this case) on the hot side have higher thermal velocities, diffusing more quickly to the cold side of the material than electrons on the cold side diffuse to the hot side. 2

Figure 1.2: Schematics of single elements of a typical thermoelectric device 4

Figure 1.3: Energy band diagram of three III-V semiconductors showing approximate estimated Fermi level positioning due to the presence of ErAs nanoparticles. 10

Figure 1.4: a) Theoretical band structure of bulk ErAs b) Relative band shifting with tensile (left of zero) and compressive (right of zero) strain on an ErAs unit cell 12

Figure 1.5: The Fermi level of GaAs and $In_{0.53}Ga_{0.47}As$ is pinned by unstrained TbAs at a universal level (black dotted line). 15

Figure 2.1: Three primary growth modes of epitaxial thin film deposition: (a) Volmer-Weber (island formation), (b) Frank-van der Merwe (layer-by-layer), and (c) Stranski-Krastanov (layer-plus-island). 19

Figure 2.2: (a) 2x (b) 4x surface reconstruction patterns visible at desorption temperature with RHEED after the native oxide layer is thermally-desorbed from a (001) GaAs wafer 22

Figure 2.3: Schematic of measurement system employing the Hall Effect. 30

Figure 2.4: Experimental setups for measurement of Seebeck coefficient at (a) room temperature at the University of Delaware and (b) under vacuum from 300-600K at the University of California, Santa Cruz 31

Figure 2.5: The 3ω method of thermal conductivity measurement is used in comparison with TDTR 34

Figure 3.1: ω-2θ XRD rocking curves of two TbAs:GaAs samples found to have 1.6% and 1.8% TbAs concentrations.. 37

Figure 3.2: The photoluminescence signal from the 1.8% TbAs:GaAs film is quenched as seen by comparison to an undoped GaAs control spectrum. 40

Figure 3.3: a) Optical absorption spectra from 1.6% and 1.8% TbAs:GaAs samples showing possible plasmon resonance peaks near 1 eV and indicating nanoparticle formation. b) The same peak is invariable under different light polarizations for the 1.8% TbAs sample, signifying possible isotropy of nanoparticle shape and distribution 41

Figure 3.4: a) HAADF STEM plan-view images of self-assembled TbAs nanoparticles in GaAs grown on (001) GaAs and viewed along the $[00\bar{1}]$ direction with an approximate layer TbAs concentration of 1.8%. b) The rock salt crystal structure of TbAs and continuous As sublattice throughout the sample are visible 43

Figure 4.1: (a) Randomly-distributed TbAs nanoparticles of about 1nm in diameter were found using plan-view HAADF STEM on 0.8% TbAs:InGaAs. (b) TbAs nanoparticles run together and lose uniformity in shape in a micrograph of 14% TbAs:InGaAs........ 47

Figure 4.2: Room temperature electrical conductivity (a), electron mobility (b), electron carrier concentration (c) and Seebeck coefficient (d) of TbAs:InGaAs are plotted as a function of TbAs concentration. 50

Figure 4.3: Room temperature thermal conductivity as measured by TDTR (a), thermoelectric power factor (b) and thermoelectric figure of merit, ZT (c), are plotted as a function of TbAs atomic concentration. 51

Figure 4.4: Electrical conductivity (a), mobility (b), and carrier concentration (c) of a few TbAs:InGaAs samples over a wide temperature range. 54

Figure 4.5: Comparison of 0.8% TbAs:InGaAs high temperature Seebeck coefficient measurements from two different measurements systems utilized for this project. 56

Figure 4.6: Thermoelectric power factor calculation ($S^2\sigma$) for TbAs:InGaAs: (a) select samples of varying TbAs concentration over a wide temperature range; (b) power factor versus TbAs concentration at room temperature and at the highest temperature for reliable measurement (600K). 56

Figure 4.7: Power factor comparison of best-performing TbAs:InGaAs, ErAs:InGaAs, and ErAs:InGaAlAs materials with a Si-doped InGaAs control sample 58

Figure 4.8: (a) Thermal conductivity data of TbAs:InGaAs and an undoped InGaAs sample, taken using the 3ω method. (b) Comparison of lattice component (electronic component subtracted) of 0.8% TbAs:InGaAs's thermal conductivity with the undoped InGaAs control sample. 59

Figure 4.9: Comparison of 3ω thermal conductivity data of best-performing TbAs:InGaAs, ErAs:InGaAs, and ErAs:InGaAlAs materials with a Si-doped InGaAs control sample 61

Figure 4.10: Thermoelectric figure of merit, ZT, as a function of testing temperature for (a) TbAs:InGaAs with varying TbAs concentrations and (b) in comparison with the same well-performing ErAs samples and Si:InGaAs control sample 62

ABSTRACT

TbAs:GaAs and TbAs:$In_{0.53}Ga_{0.47}As$ nanocomposites were fabricated and characterized for the purpose of increasing efficiency for thermoelectric power generation. An efficient thermoelectric generator will exhibit a high thermoelectric figure of merit, $ZT=S^2\sigma T/\kappa$, where S is the Seebeck coefficient, σ is electrical conductivity, T is temperature, and κ is thermal conductivity. In previous studies, ErAs and ErSb nanoparticles which precipitated in epitaxial InGa(Al)As and InGa(Al)Sb served to successfully increase ZT by reducing thermal conductivity (through phonon scattering), increasing Seebeck coefficient (through energy-dependent electron scattering), and increasing electrical conductivity (through nanoparticle donation of electrons). Theoretical predictions suggest that replacing Er with Tb at the optimum concentration will serve to further increase ZT, particularly by way of increasing the thermoelectric power factor ($S^2\sigma$).

These materials were synthesized by co-depositing Tb during III-V semiconductor growth in an ultra-high vacuum molecular beam epitaxial deposition system. At rare earth concentrations exceeding the solid solubility limit of the matrix, randomly-dispersed nanoparticles of approximately uniform size form throughout the film, as seen by scanning transmission electron microscopy. In addition, the structural, compositional, electrical, and thermal properties of the materials in both growth series (TbAs:GaAs and TbAs:InGaAs) were measured with an array of techniques.

TbAs nanoparticles in GaAs served to reduce thermal conductivity by a factor of about five with 1.8 at.% TbAs, and electrical measurements were consistent

with theoretical energy band predictions and behavior of past similar materials. The success of these TbAs:GaAs materials led the way for growth of TbAs:InGaAs which has now been shown to exhibit highly-desirable thermoelectric properties.

The room temperature thermal and electrical characterization of TbAs:InGaAs revealed a maximized room temperature power factor and ZT at a TbAs concentration of 0.3 at.%. The results were similar to those found in comparable ErAs:InGaAs materials with the exception that ErAs nanoparticles precipitated at smaller concentrations than TbAs due to an apparent increase in the solid-solubility of Tb in InGaAs. Measurements of select TbAs:InGaAs samples up to 600K revealed significant increase of power factor over similar well-performing ErAs materials and ZT reached 1.1 at 600K for 0.8% TbAs:InGaAs. This material's temperature-dependent ZT was comparable to that of the highest-ZT ErAs:InGaAs sample (0.2% ErAs); however, a major difference is that increased efficiency due to Tb is caused primarily by power factor enhancement while Er mainly served to reduce thermal conductivity. As a result, future work will involve co-depositing both Er and Tb in InGaAs in an attempt to exploit the electrical and thermal benefits each rare earth element provides, perhaps resulting in an overall very efficient thermoelectric material.

Chapter 1

INTRODUCTION

The work presented in this thesis focuses on the fabrication and properties of a series of metal/semiconductor composite materials aimed at improving efficiency for thermoelectric energy conversion. This chapter provides background information on thermoelectric materials and devices and the motivation for the engineering of rare earth/III-V semiconductor nanocomposites for thermoelectric purposes.

1.1 Thermoelectrics

1.1.1 Concepts for Thermoelectrics

Thermoelectric (TE) devices create electricity from a thermal gradient or create a thermal gradient from electricity via the thermoelectric effect. This phenomenon comprises three related effects, uncovered as a series of discoveries made primarily by Thomas Johann Seebeck, Jean-Charles Peltier, and William Thomson (Lord Kelvin) in the 19th century.[1] The Seebeck effect asserts that a potential gradient will be created across a conducting material when one side of the material is hotter than the other. Indeed, charge carriers (electrons and holes) in the material having higher thermal velocities on the hot side of the material naturally diffuse more quickly from the hot side to the cold side than in the opposite direction. If the thermal gradient across the material is maintained, flowing charge carriers build up on the cold side of the object, and this separation of charge creates a potential difference between the two

sides of the material which counters this charge imbalance. In the case that the material is part of a circuit, this voltage induces a current which be used to power a load.[1] This effect is illustrated in Figure 1.1 and essentially constitutes a conversion of thermal energy to electricity.[2] The potential difference created per degree of temperature gradient across the material is its Seebeck coefficient, S, and is material-dependent (discussed in more detail below).[1]

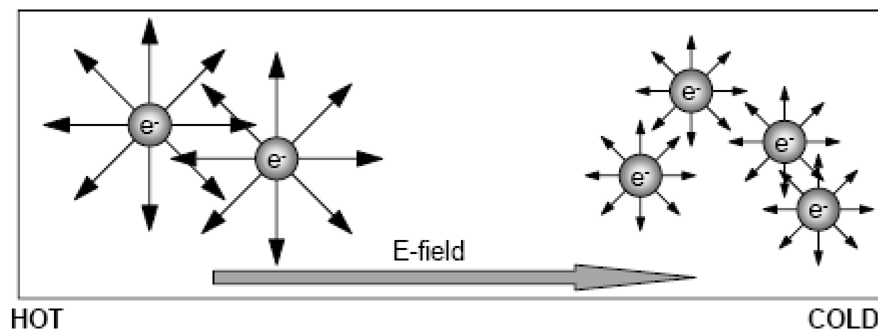

Figure 1.1: In a conductor under a thermal gradient, charge carriers (electrons in this case) on the hot side have higher thermal velocities, diffusing more quickly to the cold side of the material than electrons on the cold side diffuse to the hot side. This leaves an excess of carriers on the cold side, and a potential gradient and electric field are created across the material (image courtesy of Dr. Joshua Zide).[2]

The Seebeck effect's complement is the Peltier effect which states that when current is applied to a conducting material, a temperature difference is induced between the sides of the material where current enters and exits.[1] Flowing charge carriers carry heat from one end of the material to the other, effectively cooling one

side and heating the other. The heat transferred per unit of current applied is the Peltier coefficient, Π, is also material dependent. Lord Kelvin later discovered that the Peltier coefficient is directly related to the Seebeck coefficient by the absolute temperature at which the quantities are measured. The Thomson effect describes the heating or cooling of a homogeneous conducting material due to current passing through it as a result of a thermal gradient.[1]

1.1.2 Thermoelectric Devices and Applications

Thermoelectric devices have been created and commercialized from materials which are particularly efficient in converting thermal to electrical energy and vice versa. TE devices are useful for either generating power (by the Seebeck effect) or for localized heating and cooling (by the Peltier effect). Schematics of a typical thermoelectric device used in both ways are shown in Figure 1.2. This device is comprised of two semiconductor "legs," one n-type (majority carriers are electrons) and one p-type (majority carriers are positively-charged holes), which are connected electrically in series and thermally in parallel. When a temperature difference is maintained between the top and bottom of the legs, holes and electrons flow from hot to cold, and both legs contribute to the current which powers a load (Figure 1.2a). On the other hand, when power is supplied to this circuit, heat is transferred by flowing electrons and holes from one side of the device to the other, creating a temperature difference at opposite ends of the device (Figure 1.2b). Many of these tiny elements are connected together to provide power (thermoelectric power generators, TPG) or cooling (Peltier coolers) on a larger scale.

The possible applications of thermoelectric devices are plentiful, yet their viability depends on both their efficiency and the relative difficulty of using other

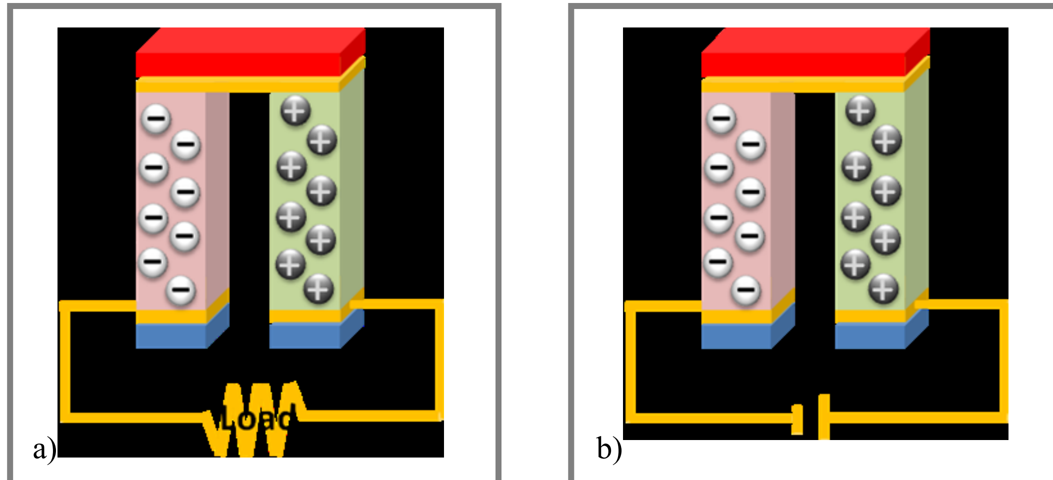

Figure 1.2: Schematics of single elements of a typical thermoelectric device. In the case of a thermoelectric power generator (a), a load is powered from a supplied temperature gradient. For a Peltier cooler (b), a hot side and a cold side are created as a result of power applied to the device.

power generation or refrigeration mechanisms. Peltier coolers have been used in small refrigerators and for cooling of small areas or objects. They are particularly useful in small spaces where other cooling mechanisms will not fit, such as inside research equipment. TPGs, on the other hand, can be useful anywhere there is a constant heat source. One can think of a plethora of applications where loss mechanisms produce waste heat. Such thermoelectric generators may be used to capture some of this lost energy, adding to the overall efficiency of the process. The practicality of their use is determined by cost-benefit analysis dependent on factors such as device efficiency, ease of integration, need for remote power generation, and cost of the heat source. Because current TPGs are not of particularly high efficiency (typically <5%)[1] and are often costly, they are generally only practical in locations where traditional power

generation is not available, such as on spacecraft. However, if TPG efficiency increases, applications in transportation (e.g., in hybrid vehicles and submarines) and in peak power generation (e.g., using waste heat from nuclear and fossil fuel power plants and possibly in conjunction with solar panels) may become accessible.

1.1.3 Thermoelectric Material Properties

There is a great deal of ongoing research in the TE field to improve material and device efficiency. The efficiency of the n- and p-type semiconducting materials comprising TE devices can be directly measured or calculated from important material properties which are individually measured. Thermoelectric materials are rated by a dimensionless figure of merit, ZT, where a higher ZT translates to higher efficiency. ZT is given by

$$ZT = \frac{S^2 \sigma T}{\kappa} \tag{1}$$

where S is the Seebeck Coefficient, σ is electrical conductivity, T is the temperature at which these properties are measured, and κ is thermal conductivity.[1] The electrical component of ZT, $S^2\sigma$, is often considered separately and is dubbed the thermoelectric power factor. The thermoelectric properties defining ZT are not independent, however, and there is an important tradeoff between all of these traits. Indeed, a low thermal conductivity is desirable for higher ZT, yet thermal conductance depends on heat transfer by both phonons and electrons, so a high electrical conductivity yields a high thermal conductivity as well. This relationship is best described by the Wiedemann-Franz law, which equates the ratio of electronic contribution to thermal conductivity to electrical conductivity to a constant (the Lorenz number) times the temperature at which these properties are measured:[1]

$$\frac{\kappa_e}{\sigma} = LT \qquad (2)$$

Furthermore, a high Seebeck coefficient necessitates a large charge separation in the material (i.e. more carriers on one side than the other), but a high electrical conductivity will cause quick and easy diffusion to negate this potential difference. High thermal conductivity also means difficulty in maintaining a high thermal gradient, also causing Seebeck coefficient to suffer. The majority of TE devices currently on the market utilize bulk semiconducting materials which are alloyed to reduce thermal conductivity, yielding $ZT \approx 1$ near room temperature. In order for TE devices to be efficient enough to enter the power generation playing field, the efficiency of the semiconducting materials must increase dramatically and over a wide temperature range. A ZT of 2 would make TE devices viable for more niche applications and a ZT of 3 would allow TPGs to compete with traditional mechanical power generators.[3]

Although electrical and thermal transport properties are naturally intertwined, epitaxial growth methods allow new materials to be engineered which aim to partially decouple these parameters. Optimizing the figure of merit involves taking a closer look at each property in ZT along with its relationship to the other properties. For example, knowing that total thermal conductivity is a summation of both electronic and phononic (lattice) thermal conductivities, and that increased electrical conductivity leads to higher electronic thermal conductivity, one concludes that in order to reduce thermal conductivity without destroying electrical conductivity, one must target the lattice contribution to thermal conductivity for reduction. One might then look for a structure which scatters phonons but not electrons. Furthermore, while increasing Seebeck coefficient and electrical conductivity simultaneously seems

oxymoronic at first, examining the theoretical origin of Seebeck coefficient provides insight into power factor optimization. The Seebeck coefficient may be described as proportional to the summation of the differential electrical conductivity of each conducting electron times its energetic distance from the Fermi level of the material divided by the total electrical conductivity:[2]

$$S = \frac{1}{qT}\frac{\int \sigma(E)(E - E_F)dE}{\int \sigma(E)dE} \quad (3)$$

where σ(E) is the energy-dependent differential conductivity of each conducting electron with energy E and E_F is the Fermi level. The absolute value of this quantity is maximized when the asymmetry of the carriers' conductivities (determined by the density of states) about the Fermi level is maximized. In a metal, where conducting electrons are energetically-distributed very evenly about the Fermi level, Seebeck coefficient is very low. However, if one could keep all of the charge carriers either above (p-type) or below (n-type) the Fermi level from conducting, this asymmetry would be maximized, yet electrical conductivity would not be greatly diminished.[2,3]

The maximum efficiency of a thermoelectric material is dependent on both the ZT and the Carnot efficiency, since thermoelectric generators and coolers are solid-state versions of heat engines. The material efficiency is given by:[1]

$$\eta_{max} = \frac{T_H - T_C}{T_H}\frac{\sqrt{1 + ZT} - 1}{\sqrt{1 + ZT} + T_C/T_H} \quad (4)$$

where T_H is the temperature of the hot side of the material and T_C is the cold side temperature. In actual TE devices, further losses result from mechanisms inherent to all electrical devices such as interconnect resistances and Joule heating along the semiconducting materials.

1.2 ErAs:III-V Nanocomposites

1.2.1 Low-dimensional Structures in Thermoelectric Materials

Fabrication of quantum dots, quantum wires, nanoparticles, nanowires, and small-period heterostructures have recently established a new realm of materials research where quantization and strain in structures cause behavior previously unseen in their bulk counterparts. The TE field is no exception to this trend where there has been resurgence in interest in the topic due to the newfound ability to alter material properties beyond the limits of traditional bulk alloys which primarily sought to reduce thermal conductivity by alloy scattering. Nearly all recent TE research has centered on utilizing nano-scale structures within semiconductors to attempt to decouple and optimize the thermoelectric properties.[3]

Nano-structures and superlattices aim first and foremost to block heat transfer by scattering more phonons than what is achievable by merely alloying. Indeed, structures larger than single atoms have larger scattering cross-sections and can scatter phonons of longer wavelengths.[4] Traveling phonons reaching a new material (air in some cases) may be scattered due to the mismatch between available vibrational modes in each material (owing to the mass mismatch between the two materials). Multi-compositional materials can also provide favorable conditions for optimization of electrical properties. Differences in band structures between two materials can create Schottky energy barriers across the interface, blocking charge carriers. Although this would enhance Seebeck coefficient while impairing electrical conductivity, tuning the height of these energy barriers can serve to strike a desirable balance between the two quantities. Recalling that Seebeck coefficient is maximized when conducting electrons have energies that are asymmetric about the Fermi level

(described above), one can theorize that an ideal barrier height would be one that blocks all of the conducting electrons on one side of the Fermi level.[2,3] For an n-type semiconductor, an energy barrier would block electrons below the Fermi level of the material. This energy-dependent scattering of electrons (or electron filtering) can serve to increase Seebeck coefficient without overly spoiling electrical conductivity and simultaneously reducing the electronic contribution to thermal conductivity. In fact, it has been shown that a maximum thermoelectric power factor can be reached with an energy barrier which is three to five times k_BT (where k_B is the Boltzmann constant and T is the temperature) above the Fermi level of the material.[5] If this task can be achieved with the engineering of nano-structures or superlattices with an appropriate combination of materials, there is great hope for large efficiency increases for thermoelectric devices. In reality, many novel materials aspiring to utilize these concepts have achieved reduction of thermal conductivity but have experienced little progress in augmenting power factor.[3]

1.2.2 ErAs Nanocomposites for Thermoelectric Power Generation

One currently-researched set of nano-structured materials seeking enhancement of thermoelectric power generation efficiency involves the co-doping of epitaxial III-V semiconductors like InGa(Al)As and InGa(Al)Sb with the rare earth metal erbium (Er). At levels exceeding the solid-solubility limit of Er in the semiconductors, randomly-distributed Er-group V nanoparticles precipitate. These semi-metallic particles have previously been shown to cause radical changes in the electrical and thermal transport properties of their host matrices.[6] In fact, ErAs and ErSb nanoparticles deposited in GaAs, GaSb, InGa(Al)Sb and InGa(Al)As semiconductors have been shown to perform tasks such as donating carriers,[7] pinning

Fermi levels,[7] reducing carrier lifetimes,[8] scattering phonons[9,10] and enhancing electron tunneling efficiency, depending on the matrix.[11]

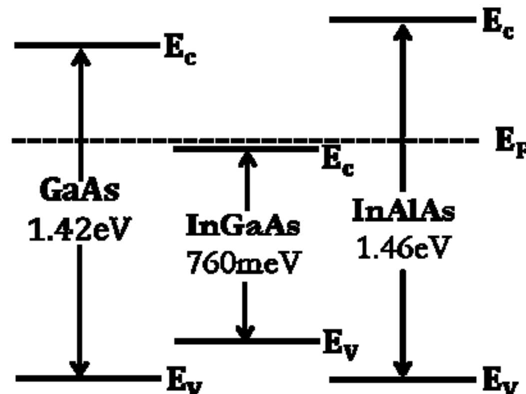

Figure 1.3: Energy band diagram of three III-V semiconductors showing approximate estimated Fermi level positioning due to the presence of ErAs nanoparticles.

TE materials are one of many applications of this type of composite system. Er-V nanoparticles serve to increase the figure of merit of the pure semiconductor for several reasons. First, the large difference in mass between Er and the group III elements in a nanoparticle that is 5-10 Er atoms in diameter reduces thermal conductivity significantly by scattering phonons and some electrons. In the case of just 0.3% (atomic) ErAs in $In_{0.53}Ga_{0.47}As$ (lattice-matched to the InP substrate), the thermal conductivity was nearly halved from that of pure InGaAs at room temperature.[12] Moreover, it has been found that these nanoparticles can donate carriers

to conduction, increasing electrical conductivity.[10] Approximately one electron is donated to conduction per ErAs nanoparticle in InGaAs.[13] Lastly, the concept of electron filtering is employed in these materials where the nanoparticles cause the Fermi level of the material to be placed ("pinned") near the conduction band edge.[14] In this way, there is a small energy barrier between the semiconductor conduction band and the nanoparticle energy level (pinned Fermi level) which causes electrons with energy below that of the Fermi level to be scattered but allows most of the electrons above the conduction band to conduct. The placement of the Fermi level in ErAs: $In_{0.53}Ga_{0.47}As$ has been both theoretically predicted (shown in Figure 1.3) and experimentally verified.[14] Alloying the InGaAs matrix with Al allows the barrier height to be tuned by Al concentration to optimize power factor (adding Al increases the band gap, primarily pushing the conduction band edge up).[14] The ErAs:III-V material system is somewhat unique in the TE field because unlike most other TE materials, not only is heat transport reduced, but the electrical properties are simultaneously improved. Progress in the development of this material system has thus far led to ZT of 1.1 at 600K for 0.2% ErAs:InGaAs and ZT of 1.33 at 800K for 0.6% ErAs:InGaAlAs.[14,15]

1.2.3 TbAs:III-V Nanocomposites

The progress made in thermoelectric power generation efficiency with the ErAs:III-V materials system has opened doors to explore the properties of other rare earth metal/semiconductor composites for thermoelectric and other applications. The work presented in this thesis focuses on the effects of terbium arsenide nanoparticles in III-V semiconductors, particularly TbAs:GaAs and TbAs:InGaAs, in light of their potential for thermoelectric applications. There are several reasons outlined below

which explain why TbAs nanocomposites are expected to provide efficiency enhancement over similar ErAs and ErSb materials.

1.2.3.1 Properties of Rare Earth Monopnictides

Even though very little has been published about TbAs and most other rare earth monopnictide compounds, there is a good deal of information available on the properties and synthesis of ErAs and its role in III-V semiconductors, as these materials have proven to be useful for other applications. With the exception of a few europium compounds, the rare earth monopnictides are all known to form the NaCl rocksalt crystal structure with lattice parameters which vary from 4.8Å - 6.6Å.[16] As the atomic number of the rare earth metal increases, the lattice constant decreases (this is known as the Lanthanide contraction). It is convenient that many of these compounds are nearly lattice-matched to several other technologically-important semiconductors

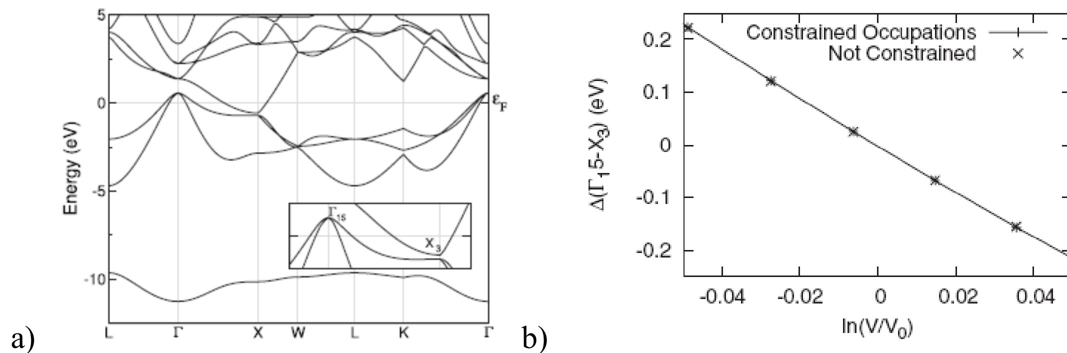

Figure 1.4: a) Theoretical band structure of bulk ErAs b) Relative band shifting with tensile (left of zero) and compressive (right of zero) strain on an ErAs unit cell (both images reprinted from [16] with authors' permission, copyright (2008) by the American Physical Society).

like GaAs (5.65Å) and InP (5.87Å).

Because the increase in valence electrons with increasing rare earth atomic number occurs in the f-shell, which is tightly-bound to the core of the atom, it is not expected that the electronic properties of the compounds will vary greatly while only varying the rare earth species.[17] Indeed, the electrical resistivity of bulk TbAs has been measured to be 1.8×10^{-3} Ω-cm (similar to 7.2×10^{-3} Ω-cm for bulk ErAs), and its Seebeck Coefficient is +18 μV/°C (versus +16 μV/°C for ErAs).[18] ErAs is known to be a semimetal in its bulk form, and its calculated band structure is shown in Figure 1.4a.[17] TbAs is also expected to be a semimetal as a single crystal, but this fact is still unverified and there is reason to believe it may be a semiconductor.[16] Furthermore, in the case of these nanocomposites where ErAs and TbAs are in the form of 1-3nm diameter nanoparticles, it is likely that the effect of strain on the nanoparticles from the surrounding matrix will dominate changes in their electronic properties rather than the specific rare earth element. Strain (hydrostatic pressure) can cause the relative and absolute band energy levels to shift, at times causing a band gap to open or close and converting a semimetal to a semiconductor or vice versa. The shift of the conduction (X_3) and valence (Γ_{15}) bands relative to each other as a function of unit cell deformation (cell volume as a fraction of bulk cell volume) for ErAs is shown in Figure 1.4b.[17]

1.2.3.2 Power Factor Enhancement with TbAs Nanoparticles

TbAs nanoparticles are expected to provide certain benefits over ErAs, due primarily to their lattice larger constant (5.815Å vs. 5.734Å for ErAs)[19] which is anticipated to favorably alter the nanocomposites' electrical properties while providing similar reduction in thermal conductivity. It has been observed both

theoretically and experimentally that strain of the nanoparticles brought about by lattice-mismatch to the semiconductor is the major factor in the positioning of the Fermi level within the semiconductor's band gap.[14,17] Indeed, tensile strain on the nanoparticles relative to the matrix causes the Fermi level to be shifted up from a universal donor level, determined by the work function of the rare earth arsenide, towards the conduction band while compressive strain causes it to be shifted down towards the valence band.[17] Although we believe this trend to be true, it is very difficult to calculate the exact energy levels theoretically;[20] therefore, seeking experimental evidence is more useful. ErAs was predicted and experimentally observed to pin the Fermi level of $In_{0.53}Ga_{0.47}As$ and InP lattice-matched InGaAlAs (up to ~20% Al) above the conduction band;[14] this is attributed to the tensile strain of the nanoparticle in the matrix. Given that the electronic properties of TbAs are expected to be very similar to those of ErAs (discussed above), TbAs should pin the Fermi level near the same universal donor level as ErAs in its unstrained state. However, the ~3% compressive strain of TbAs in GaAs is predicted shift the Fermi level TbAs:GaAs down to near mid-gap (Figure 1.5). Though this would render TbAs:GaAs a poor TE material, this largely-unexplored class of materials may open doors for a variety of other applications. Therefore, several TbAs:GaAs samples were grown and characterized, proving themselves useful for determining the structural, electrical, and thermal changes that TbAs nanoparticles might bring about in this and other III-V semiconductors.

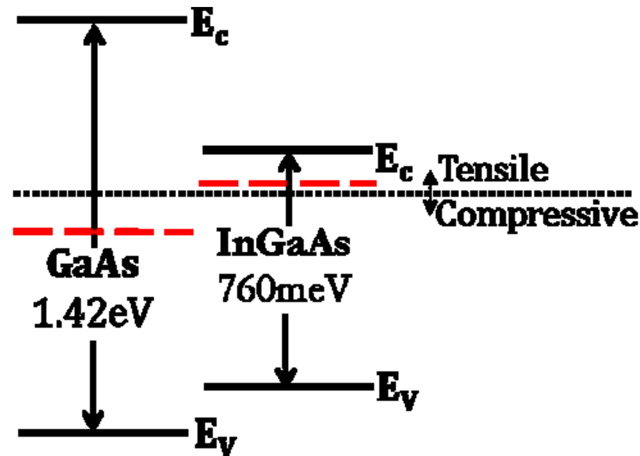

Figure 1.5: The Fermi level of GaAs and $In_{0.53}Ga_{0.47}As$ is pinned by unstrained TbAs at a universal level (black dotted line). This level is shifted upwards if the nanoparticle is tensilely strained or downwards if the nanoparticle is compressively strained. Red dashed lines indicate the estimated Fermi level of GaAs and InGaAs with TbAs nanoparticles.

Alternatively, TbAs, which is less strained than ErAs in $In_{0.53}Ga_{0.47}As$ at ~0.9% tensile mismatch, is expected to pin the Fermi level slightly below the conduction band. We roughly estimate the barrier height (an energetic well also acts as a barrier) between the TbAs nanoparticles and InGaAs conduction band edge as about 65 meV, but this calculation is based solely on the shifting of ErAs's Fermi level due to strain. If the Fermi level of TbAs:InGaAs is indeed slightly below the conduction band edge, results should show an enhanced Seebeck coefficient and reduced electrical conductivity over ErAs:InGaAs, likely resulting in a higher power factor. Both Seebeck coefficient and electrical conductivity are expected to increase with rising temperature, so these materials should perform best for thermoelectrics at

higher temperatures. An additional benefit of the TbAs:InGaAs system is that the small lattice-mismatch between the nanoparticle and the matrix should allow samples grown to exhibit fewer long-range defects caused by relaxation of the strained layer, possibly leading to better uniformity and longer lifetimes in these composites.

1.3 Overview of Thesis

In this project, these theories regarding the advantages of TbAs nanoparticles embedded in III-V semiconductors for the improvement of efficiency in thermoelectric power generation were tested in two series of growths by molecular beam epitaxy. The details of the growth method and characterization techniques employed are described in Chapter 2. The first series, outlined in Chapter 3, focused on depositing TbAs nanoparticles in GaAs in order to study the fundamental properties of TbAs nanoparticles as well as the thermal and electrical properties of this nanocomposite. The second series, found in Chapter 4, involved the growth of $In_{0.53}Ga_{0.47}As$ with TbAs nanoparticles. These samples were characterized at room temperature and over a wide temperature range as a function of TbAs atomic concentration ranging from 0% to 5%. The electrical and thermal transport properties are reported along with the structural and compositional properties. Thermoelectric power factor and figure of merit are calculated, and the highest efficiency TbAs:InGaAs material is compared to other well-performing nanocomposites. Conclusions are drawn and future directions for further exploration of this materials system are outlined in Chapter 5.

Chapter 2

EXPERIMENTAL METHODS

The novel materials for this project were fabricated by molecular beam epitaxy (MBE) at the University of Delaware. Each sample grown was characterized for structural, electrical, and thermal properties and analyzed for possible application to thermoelectric and other devices. Structural and compositional characterization was performed with x-ray diffractometry (XRD), Rutherford backscattering spectrometry (RBS), optical absorption spectroscopy, and plan-view high-angle annular dark-field scanning transmission electron microscopy (HAADF STEM). Resistivity, Hall effect, and Seebeck coefficient measurements provided the electrical characterization of each sample at room temperature and over a wide temperature range. Photoluminescence (PL) was also employed for one type of material. Finally, thermal conductivity was determined by time-domain thermoreflectance (TDTR) and the 3ω technique. This chapter gives an introduction to MBE and to each of these techniques as well as to the conditions under which the materials for this project were fabricated and measured.

2.1 Growth of Materials by Molecular Beam Epitaxy (MBE)

MBE was chosen as the method of fabrication for these nanocomposites due to its ability to produce extremely high-quality materials with very few unwanted impurities and defects. A low-defect material provides better electrical performance and makes it easier to recognize the effects of altering growth parameters on material

properties. Such quality is mostly dependent on the purity of the source materials and the ultra-high vacuum (UHV) environment under which MBE operates.

At a basic level, MBE growth employs simple thermal evaporation of very high-purity source materials onto a single-crystal substrate where atoms or single-element molecules meet and chemically react with each other. Each solid or liquid source material is kept in a non-reacting crucible in an effusion cell at a certain distance and angle away from the substrate. The effusion cell serves to heat the source material accurately to provide an exiting vapor pressure which can be measured and correlated to a growth rate on the substrate surface. The low background pressure (typically ~10^{-10} Torr) of the UHV environment, provided by a combination of ion, cryo-, and/or turbo pumps and liquid nitrogen-filled "cryopanels," causes the mean free path of the atoms/molecules exiting the effusion cells to be longer than the distance between the cells and the substrate. This allows nearly all atoms/molecules to reach the surface directly from the cell without reacting with other species along the way, creating an effective "beam" of atoms or molecules from each source.[21]

Because the constituent atoms generally only react at the surface, local thermodynamics and surface kinetics rule the formation of material "growing" outwards from the substrate, which is rotated to provide even surface coverage by arriving atoms. This formation of the materials at the scale of a few monolayers at a time means that thermodynamic equilibrium as a whole is not realized during growth, allowing structures to be engineered that are out of reach with other thermal deposition and bulk synthesis tecnniques.[21] This allows the grown film to be epitaxial, or arranged in the same structure as the underlying monocrystalline substrate, and the composition change at the interface to be abrupt and laterally smooth. The

temperature of the substrate determines the favorable atomic configurations and rate of diffusion of surface atoms, leading to different possible growth modes at the surface (shown in Figure 2.1). Given the ability to control the stoichiometric ratio of atoms impinging upon the surface and the thermal energy of the reacting atoms, nearly any stable or metastable structure involving the available sources may be formed with this technique. Furthermore, because the beams are able to be turned on and off at any time during growth with the opening and closing of a shutter covering the mouths of the effusion cells, material composition can be altered during growth, allowing the formation of heterostructures and superlattices.[21]

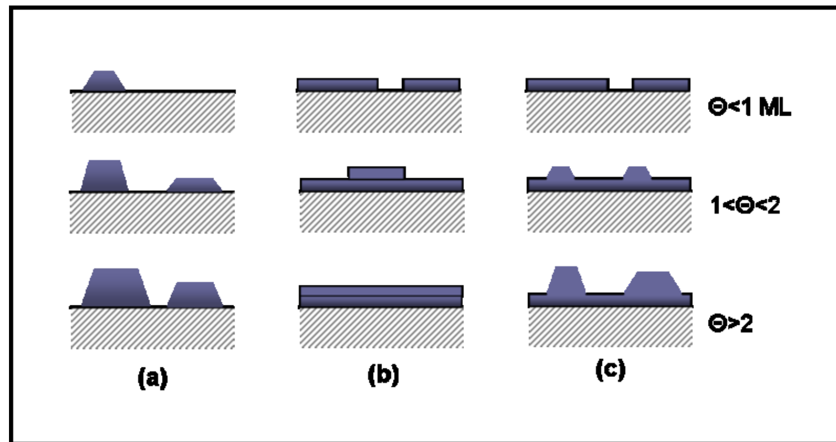

Figure 2.1: Three primary growth modes of epitaxial thin film deposition: (a) Volmer-Weber (island formation), (b) Frank-van der Merwe (layer-by-layer), and (c) Stranski-Krastanov (layer-plus-island).[22]

The materials presented here were grown with an OSEMI NextGEN solid-source MBE system housed in a Class 10,000 clean room. Like most MBE systems, a complex array of appendages to the main growth chamber provides exceptional material quality control over other thermal evaporation techniques. A substrate wafer first enters the MBE through a loading chamber and is then moved to a preparation (prep) chamber before entering the growth chamber (all of which are separated by sealing gate valves), being thermally-cleansed at each step along the way. Wafers are baked to evaporate impurities on the surface at a low temperature (~50°C) in the loading chamber, then for two hours at 325°C-350°C in the prep chamber, and finally at 400°C for 20 minutes once in the growth chamber. While most stray atoms are pumped out, a residual gas analyzer (RGA) mass spectrometer attached to the growth chamber allows monitoring of the quantity of each species present in the system. Even after baking wafers, the surfaces still harbor a native oxide which must be thermally-desorbed before anything can be grown onto the pure crystal underneath. Reflection high-energy electron diffraction (RHEED) is used *in situ* to monitor this oxide desorption as well as the growth itself. The shallow angle between the electron beam and substrate as well as the short electron wavelength (less than typical crystal lattice parameters) allow the reconstruction of the surface during desorption and growth to be interpreted in reciprocal space. With the particular substrates used in this project, InP and GaAs, oxide desorption is confirmed when a 2x4 spot pattern (Figure 2.2) becomes visible on the phosphoric RHEED screen, corresponding to the known surface reconstruction of InP and GaAs (zinc-blende crystals) at the desorption temperature. Furthermore, during growth, the growth mode and surface morphology may be monitored with RHEED; a “streaky” RHEED pattern corresponds to two-

dimensional layer-by-layer growth while a "spotty" (broken up streaks) pattern indicates three-dimensional growth of islands, and chevrons indicate facets on the surface.[2] During the nanoparticle/III-V growths presented here, RHEED patterns signified three-dimensional growth, similar to the patterns observed in analogous ErAs:III-V growths.[2] Growths are automated with the commercial program AMBER which controls the shutters and cell temperatures from an input recipe. In addition to observing RHEED patterns, the user controls the substrate temperature and substrate rotation manually during the growth.

While the MBE used houses ten source materials, only five were needed for these growths: In, Ga, As, Er, and Tb. The In source is a VEECO SUMO effusion cell, and the Ga source is an e-science valved Titan effusion cell with a SUMO-like crucible (cylindrical with conical opening). Both are heated at the base and tip of the crucible. The terbium and erbium sources are e-science high temperature effusion cells with conical tungsten crucibles (tantalum forms a eutectic with Er and Tb). Finally, the As source is a VEECO valved cracking effusion cell where sublimated As_4 splits to As_2 while passing through a high-temperature cracking tube before entering the growth chamber. The atomic fluxes of the beams of source material are measured by the beam equivalent pressure (BEP) on an ion gauge mounted opposite the substrate holder, which faces the sources when turned around. Flux is simple to calculate from BEP with the Hertz-Knudsen equation (below), and the typical As to group III flux ratio used in these growths was about 100:1.

$$Flux = \frac{1}{A}\frac{dn}{dt} = \frac{\alpha p}{\sqrt{2\pi mkT}} \tag{5}$$

Here, A is the cross-sectional area measured, dn/dt is the number of particles arriving at the area per unit time, α is an material-dependent evaporation coefficient, p is the BEP as measured by the ion gauge beam flux monitor (BFM), m is the mass of a single particle, k is the Boltzmann constant, and T is the temperature.[21]

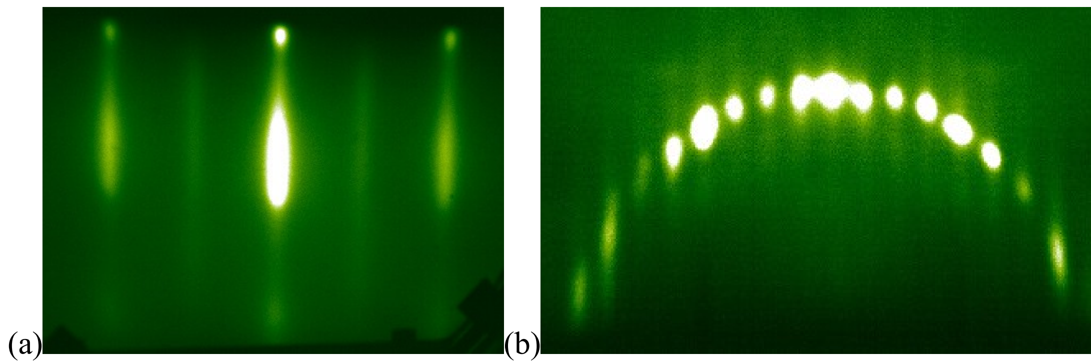

Figure 2.2: (a) 2x (b) 4x surface reconstruction patterns visible at desorption temperature with RHEED after the native oxide layer is thermally-desorbed from a (001) GaAs wafer (image courtesy of Dr. Hong Lu, unpublished).[23]

In order to form the TbAs and ErAs nanoparticles, Tb and/or Er are co-deposited with the III-V sources at a growth rate which is a fixed fraction of the III-V growth rate. At concentrations above the solid-solubility limit of Tb or Er in (In)GaAs, nanoparticles precipitate randomly throughout the material. This precipitation was previously shown to occur in the case of GaAs and InGaAs co-deposited with erbium.[2,24,25] The nanocomposites were grown at rates of 0.6-1.5 μm/hr, and total film thicknesses ranged from 0.25 μm to 1 μm. No differences in

electrical or thermal properties were noted where growth rate or film thickness varied. Both the GaAs and InGaAs nanocomposites were grown with a substrate temperature of 490°C, as measured by band-edge thermometry (BET), a technique which sensitively measures the narrowing or broadening of the band gap of the substrate with changing temperature by detecting light transmission through the wafer. It has been observed that substrate temperature can have an effect on the size of the nanoparticles (higher temperature results in larger particles).[26,27]

In the case of the TbAs:GaAs materials, a 50nm undoped GaAs buffer layer was grown before the active layer to smooth the surface of the undoped (001) GaAs substrate, but no capping layers were grown. Several different Tb source temperatures were used, corresponding to different concentrations of TbAs nanoparticles, but the two main samples whose results are discussed in Chapter 3 were grown with Tb temperatures of 1320°C and 1345°C .

For the TbAs:InGaAs materials, Tb was deposited with $In_{0.53}Ga_{0.47}As$, which is lattice-matched to the (100) InP:Fe semi-insulating substrates. Flux ratios corresponding to lattice-matched InGaAs composition were calibrated using x-ray diffraction (XRD). All but 3 of the 20 TbAs:InGaAs samples were grown with a 100nm $In_{0.53}Ga_{0.47}As$ buffer layer in an attempt to enable post-growth comparison of the compositions of the buffer and active layers using XRD. About half of the samples were grown with a 1 μm thick TbAs:InGaAs layer while one sample was 500nm and the remaining were 250 nm in thickness. The main variable in this growth series was the concentration of TbAs nanoparticles in InGaAs. Varying the Tb effusion cell temperature (1100°C-1480°C) yielded concentrations of 0.06% to 14% TbAs. Several InGaAs and Si-doped InGaAs control samples were grown and characterized as well.

It has proven very difficult to measure the flux of Tb from beam-equivalent pressure (BEP) measurements. The probable cause of the flux measurement problem is the low vapor pressure of Tb at the temperature of the filament of the beam flux monitor ion gauge, causing Tb to stick to the filament and preventing accurate flux measurements. Because of this challenge, an attempt was made to calibrate TbAs concentration as a function of Tb effusion cell temperature using Vegard's Law, which states that the lattice constant of a two-constituent material scales linearly from one constituent's lattice constant to the other's as the concentration of the second constituent increases. Using this principle, a linear interpolation between the lattice constant of TbAs and the semiconductor matrix yields a percentage of TbAs corresponding to the lattice constant of the film, as calculated using Bragg's Law from XRD data. It was later revealed by Rutherford backscattering spectrometry (RBS) that actual TbAs concentrations were much lower than was expected using the above method due to a superdilation of the lattice constant by TbAs nanoparticles, as was noted in ErAs:GaAs.[28,27] After this discovery, TbAs growth rates were calibrated by RBS measurements of previous samples, and confirmed or adjusted with RBS measurements of current samples. The exact composition of the InGaAs varied somewhat as well, due to a slight instability in the flux from the In effusion cell. RBS measurements showed a deviation in In and Ga content of up to ±2% from the percentages corresponding to InP lattice-matching.

2.2 Sample Characterization

As was discussed in the first chapter, the thermal and electric transport properties are central to thermoelectric material performance. As well, structural and compositional information gathered about the materials can give insight into the

physical mechanisms causing these macroscopic properties. Accordingly, each sample grown was characterized with an array of techniques to illustrate its physical and thermoelectric features.

2.2.1 Structural Properties

Structural information was obtained through several techniques including XRD, RBS, optical absorption spectroscopy, and HAADF-STEM. XRD spectra revealed the lattice constant, thickness, and qualitative observation of degree of crystallinity of the materials. Using a high-resolution PANalytical X'Pert PRO Materials Research Diffractometer at the University of Delaware, ω-2θ rocking curves were taken around the (004) GaAs or (004) InP reflections, depending on the substrate, in a triple crystal configuration (the first crystal being a four-bounce Ge (220) monochromator and the third a three-bounce Ge (220) analyzer crystal). The x-ray source was the 1.54Å wavelength $K_{\alpha 1}$ emission line of Cu. If the film thicknesses were below a critical thickness, estimable by:

$$h_{crit} = \frac{{a_{sub}}^2}{|a_{film} - a_{sub}|} \tag{6}$$

where a_{film} is the bulk lattice constant of the film material and a_{sub} is the lattice constant of the substrate, constructive interference fringes between the top of the strained film and the top of the layer below were visible. From these thickness fringes, the thickness of the film could be calculated using Bragg's Law:

$$n\lambda = 2dsin\theta \tag{7}$$

where n is the difference in fringe numbers, counting outward from the 0 layer peak, between two fringes which are being compared (n=1 for two adjacent fringes), λ is the x-ray source wavelength, d is the thickness to be determined, and θ is the angle of one

fringe peak relative to the other. Films with thicknesses greater than the critical thickness relaxed through the formation of defects in the film which cause destructive interference. The lattice constants of the films were also calculated using Bragg's Law, where n=4 due to the measurements being taken around the (004) reflections, d corresponds to the lattice constant, and θ is the absolute angle at which the layer peak occurs. Finally, a material exhibiting thickness fringes and having a relatively narrow full width at half-maximum (FWHM) (≤0.05° or 180 arcsec ω) was considered to have very uniform crystallinity. The GaAs films overall were better quality materials due to the automatic lattice matching of GaAs to the GaAs substrate so that the only strain in the layer was due to the nanoparticles; on the other hand, since the InGaAs was not always perfectly lattice-matched to InP due to the slight instability of the In effusion cell, the semiconductor matrix added strain to the system in addition to the nanoparticles, leading to a small critical thickness in some cases (less than 500nm).

As explained earlier, TbAs concentrations were determined from RBS and compared to XRD results. Film thicknesses are also able to be gathered from RBS spectra, and those found compared well with those obtained from XRD thickness fringes. RBS analysis was performed at the Rutgers University Tandem Accelerator using 2 MeV He++ ions in a vacuum chamber at a pressure of $\sim 10^{-6}$ torr. A typical Si surface-barrier detector with an energy resolution of about 17 keV was placed at a 163° scattering angle. Ion beam current on the sample was 10-20 nA, and the beam spot was about 2mm in diameter. Data was collected until 10μC of charge accumulated (10-15 min). RBS data analysis was performed by fitting spectra using the commercial program SIMNRA. Not all samples were analyzed with RBS; calibrations were performed with about eight TbAs:GaAs samples, and a few samples

from each of the following growth series were measured to confirm the estimated concentrations.

Optical absorption spectroscopy (OAS) was performed on the first Tb-containing nanocomposites grown, TbAs:GaAs, at the University of California at Santa Barbara (UCSB). The idea was based on interesting absorption properties found to occur in previous nanocomposite materials where plasmon resonance peaks were found to occur at energies smaller than the bandgap in GaAs containing ErAs nanoparticles.[27] Since no data had yet been gathered confirming or denying the existence of nanoparticles in TbAs:GaAs, OAS was employed to speculate on their presence. Spectra were obtained with a Cary 500 spectrophotometer in a range of 800 to 3000 nm with a 1 nm data interval. The absorption coefficient was calculated as

$$\alpha = -\frac{1}{t} ln\left(\frac{T}{T_0}\right) \tag{8}$$

where T is the transmission through the measured sample, T_0 is the transmission through a bare undoped GaAs substrate sample, and t is the thickness of the active TbAs:GaAs epilayer.[27]

Plan-view HAADF STEM was later performed at UCSB in order to visualize the structure and confirm the compositions of the TbAs:GaAs and TbAs:InGaAs materials. The samples were prepared by mechanical polishing without the use of Ar^+ milling. A FEI Titan 80-300 STEM/TEM equipped with a field-emission electron gun operated at 300 kV was used.

2.2.2 Electrical Properties

The electrical resistivity, mobility, and carrier concentration of all grown materials were measured with a resistivity/Hall Effect measurement system at UD. For room temperature measurements, van der Pauw sample geometry was employed by soldering ohmic indium contacts to the corners of samples which were cleaved to roughly 1cm x 1cm squares. For wide temperature measurements, taken in a cryostat capable of reaching 20K-800K, van der Pauw patterns were processed by first performing a mesa etch to the substrate on an approximately 7mm x 7mm piece of sample, then passivating the surface with 150nm of SiN followed by 300nm of SiO_2 by plasma-enhanced chemical vapor deposition (PECVD) in order to avoid group V sublimation at higher temperatures. Next, the areas at the four corners of the film designated for contact pads were etched to the substrate before 40nm of Ti followed by 400nm of Au were deposited onto the areas by e-beam evaporation.

In order for the van der Pauw method to be effective, these conditions must be met: the conducting medium must be very thin in comparison to its lateral dimensions, the sample must be as symmetrical as possible, there must not be any isolated holes in the sample, and the substrate must be much more resistive than the layer to be measured – otherwise, current will also flow through the substrate and the measurement will include contributions from both parts.[30] Nonetheless, both the InP:Fe and undoped GaAs substrates used were very resistive in comparison to the thin films. In this method, current is supplied between two adjacent contacts, and voltage is measured between the other two. Current-voltage curves are taken along this and each of the other edges, where the slopes of the curves are the resistance in each direction. In-plane sheet resistance, R_s, can then be calculated as

$$R_s = \frac{\pi R}{ln2} = \frac{\rho}{t} \quad (9)$$

when the resistance (R) in both lateral directions is approximately equal (these materials were expected to be nearly isotropic). This measurement method subtracts out any contact resistance so that sheet resistance is only that of the film itself. In-plane resistivity of the film, ρ, is then calculated as the product of the sheet resistance and the thickness (t) of the film.[30]

Carrier concentration and mobility were measured in the nanocomposites using the Hall Effect in the same experimental setup. In these measurements, a magnetic field, provided by an electro-magnet capable of up to 3000 Gauss, was applied in the cross-plane direction of these n-type samples while a small current was passed from one side to the other. The field causes the electrons to initially move orthogonally to the magnetic field and current directions according to the Lorentz force, which creates an electric potential (Hall voltage) across the material that in turn causes drift in the opposite direction (Figure 2.3). This is called the Hall Effect, and this Hall voltage can be measured across the sample, perpendicular to the current flow. The carrier concentration is calculated from the following relationship:[31]

$$n = \frac{1}{qtR_{Hall}} = \frac{IB}{qtV_{Hall}} \quad (10)$$

where q is the elementary charge, t is the sample thickness, and R_{Hall} is the Hall resistance measured as the slope of a voltage (V_{Hall}) vs. current (I) x magnetic field curve (B). Finally, mobility is calculated by its relationship with conductivity, σ, and carrier concentration:[31]

$$\sigma = \frac{1}{\rho} = q\mu n \tag{11}$$

Seebeck coefficient was measured at room temperature with a two point voltage measurement at either end of an approximately 5mm x 15mm bar of the sample material. Thermocouples at each end of the bar measured the temperature difference which was created with two oppositely-powered Peltier coolers upon which the ends of the bar rested (Figure 2.4a). Silver paste provided ohmic contacts for the electrical probes as well as good thermal contact between the sample and Peltier coolers and the sample and thermocouples. At least five data points were taken for

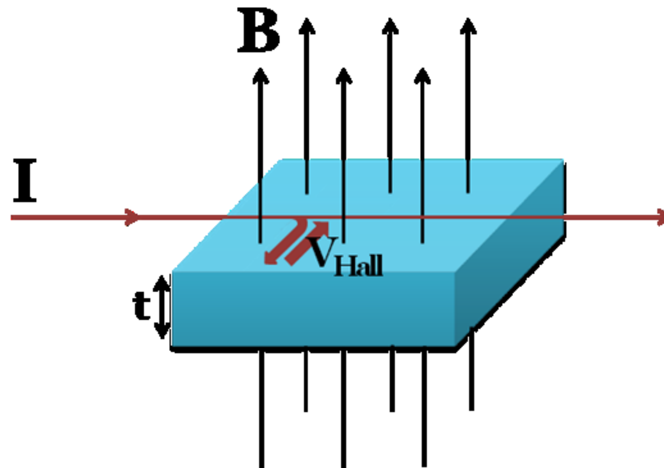

Figure 2.3: Schematic of measurement system employing the Hall Effect. A magnetic field (B) is passed through the sample, orthogonal to a current across one lateral direction of the film. The Hall voltage created to oppose the Lorentz force due to the magnetic field on the charge carriers is measured.

each sample to reduce error, and the slope of the plotted data was the average Seebeck coefficient for each. Again, if the resistivity of the substrate is much greater than that of the thin film (as was the case for the wafers used), any influence from the substrate on Seebeck coefficient measured may be safely neglected.

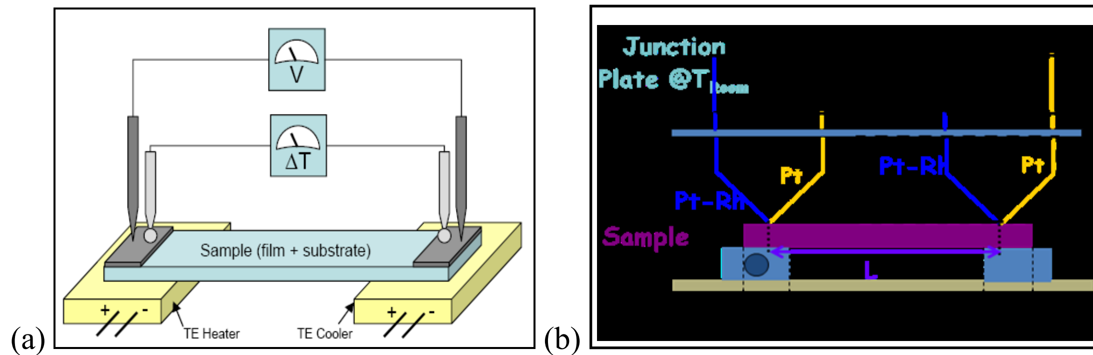

Figure 2.4: Experimental setups for measurement of Seebeck coefficient at (a) room temperature at the University of Delaware (image courtesy of Dr. Joshua Zide)[2] and (b) under vacuum from 300-600K at the University of California, Santa Cruz (image courtesy of Tela Favaloro, unpublished).

High temperature Seebeck coefficient measurements were made at UCSB and the University of California at Santa Cruz (UCSC). Seebeck bars of either 5x15mm (UCSC) or 12x15mm (UCSB) were processed in the same manner as the van der Pauw high temperature samples, with Ti/Au contacts and SiN/SiO_2 passivation. Samples are mounted inside a vacuum chamber where each end rests on a boron nitride stage, one of which contains a cartridge heater to induce a temperature gradient

across the sample. Voltage and temperature are measured at the same point on both ends of the sample with the same probes. Four nano-voltmeters are used to simultaneously measure the temperature at each side from type R thermocouples and the voltage across the sample, subtracting out the voltage added by the platinum leads (Figure 2.4b). Six data points, which are an average of 100 measurements each, are plotted at each temperature to reduce error in the average Seebeck coefficient. Measurements were taken approximately every 50 degrees from 300-600K.

Finally, photoluminescence (PL) measurements were utilized for studying the electrical properties of TbAs:GaAs nanocomposites. In particular, PL provided the opportunity to observe if these materials behaved consistently with theoretical predictions of TbAs nanoparticles pinning the Fermi level deep within GaAs's band gap, as discussed in Section 1.2.3.2. In a material with few electrical states within the band gap, there should be a strong PL signal at the wavelength corresponding to that band gap's energy; on the other hand, a quenched PL signal would signify a significant number of deep states present within the band gap which cause carriers to recombine non-radiatively. PL was acquired from a 1.8% TbAs:GaAs sample using an Acton Spectrophotometer, illuminated with a Mira 900P pulsed titanium-sapphire laser at 800nm. This was compared with the PL signal collected from the back of the same GaAs wafer on which this sample was grown.

2.2.3 Thermal Properties

Low thermal conductivity is vital for the performance of a thermoelectric material, as was discussed in Chapter 1. Two different methods of measuring thermal conductivity were utilized for this project and described below: room temperature thermal conductivity was measured by time-domain thermoreflectance (TDTR) at

UCSC, and thermal conductivity over a wide temperature range was measured with the 3ω technique at the University of California at Berkeley (UCB).

In preparation for TDTR measurements, the sample surfaces were cleaned with acetone followed by isopropyl alcohol, DI water, and a 40 second buffered HF dip to remove any oxide. Following this cleaning, a ~50nm layer of pure Al was deposited on the surface of the samples by e-beam evaporation. For the measurement, a femtosecond laser pulse is split in two beams for pumping and probing. The pump pulse heats the Al surface, and the delayed probe pulse measures the reflectivity of the surface as a function of time as the heat diffuses into the thin film. Cross-plane thermal conductivity is estimated by fitting the experimental thermoreflectance data with a 3D thermal model based on thermal quadrupoles. More detailed explanations can be found elsewhere.[32, 33]

TDTR was compared with a second technique of thermal conductivity measurement, the 3ω method, which also provided high temperature results. Unlike TDTR and other thermal conductivity measurement techniques, the 3ω method measures frequency response rather than time response of heat flow. For this reason, the effect of radiative heat losses over time is minimized.[34] While TDTR was performed on all samples, 3ω was only performed on a few InGaAs samples of varying TbAs concentrations due to the labor-intensive sample preparation necessary for 3ω and also because about half of the samples grown did not meet film thickness requirements for accurate measurements with this method (at least 1 μm).

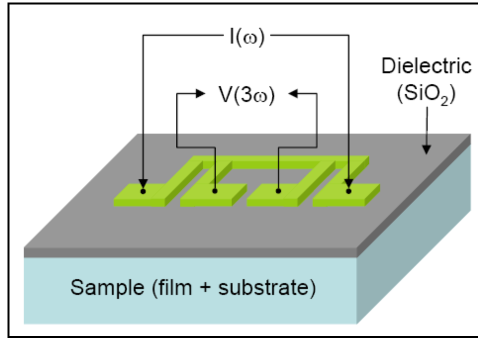

Figure 2.5: The 3ω method of thermal conductivity measurement is used in comparison with TDTR. A dielectric layer and Pt/Zr wires are deposited on the sample surface for measurements (image courtesy of Dr. Joshua Zide).[2]

A schematic of the sample processing design and 3ω measurement technique can be found in Figure 2.5.[2] Samples are prepared by first depositing a 100-300 nm dielectric layer on the surface of the film. Either SiO_2 or Al_2O_3 is deposited by low temperature oxide growth (LTO) or atomic layer deposition (ALD), respectively. Afterwards, metal lines, typically 600 μm long and 10 μm wide, are patterned lithographically on top of the dielectric, and metal wires are formed by depositing 200 nm of platinum followed by 5 nm of zirconium in the lines which are first cleaned for one minute with oxygen plasma in order to improve adhesion between the dielectric and metal layers. Finally, the samples were annealed at 550°C for 3 minutes to avoid a discontinuity which would otherwise typically occur in electrical measurements around 700K.

The 3ω method is so-named for the quantity measured when a sinusoidal current of ω is applied across the metal wire on the surface. The current serves to heat the sample at a frequency of 2ω by Joule heating ($P_{loss} = I^2R$) at the second harmonic.

Furthermore, since the resistance of the metal wire changes with temperature, it also changes at a frequency of 2ω. This 2ω resistance times the applied current at ω results in a voltage across the wire which varies with frequency 3ω. Using this voltage and the resistance of the wire as a function of temperature, the temperature drop across the sample underneath the metal is able to be determined. Using this information which is gathered from both the thin-film sample and a reference sample (substrate and buffer layer, if applicable), thermal conductivity of the active layer is extracted using the differential method.[35]

Chapter 3

TbAs:GaAs NANOCOMPOSITES: RESULTS AND DISCUSSION

3.1 Characterization of TbAs:GaAs Nanocomposites

Based on the effects of nanoparticle formation in Er-containing systems and their success as thermoelectric (TE) materials,[7,10] similar terbium arsenide/III-V nanocomposite systems are expected to behave similarly. In this chapter, the results of the characterization of TbAs:GaAs nanocomposites are reported and analyzed. Although TbAs:GaAs is expected to perform poorly as a thermoelectric material, this new materials system may open doors for a variety of other applications, and these samples are therefore useful for determining the structural, electrical, and thermal changes that TbAs nanoparticles will bring about in other III-V semiconductors. Further theoretical details and motivation for growing these materials are given in Section 1.2.3.2, and details of the growth and characterization methods are given in Chapter 2. As a reminder, TbAs was co-deposited with GaAs by molecular beam epitaxy (MBE). Several TbAs:GaAs thin film samples were grown, but only two were analyzed extensively. All growth conditions were identical for both samples with the exception of the terbium source temperature, which was 1320°C for one sample and 1345°C for the other.

The TbAs:GaAs materials were characterized with several techniques including x-ray diffraction (XRD), Rutherford backscattering spectrometry (RBS), resistivity measurements, photoluminescence (PL), time-domain thermoreflectance

(TDTR), optical absorption spectroscopy (OAS) and plan-view high-angle annular dark-field scanning transmission electron microscopy (HAADF STEM).

3.1.1 Structural Properties

Several important observations about the structure and composition of the TbAs:GaAs samples grown were gathered from XRD and RBS. XRD spectra of the two samples grown are shown in Figure 3.1. Initially, the atomic concentration of TbAs in the films was calculated from the position of the film peaks in the ω-2θ rocking curves. This was done by first calculating the lattice constant of the thin film

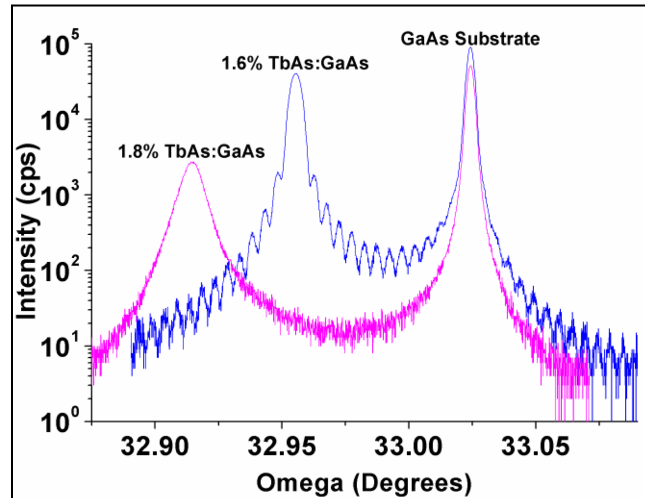

Figure 3.1: ω-2θ XRD rocking curves of two TbAs:GaAs samples found to have 1.6% and 1.8% TbAs concentrations. Fringes on the 1.6% sample were used to calculate film thickness, and the FWHM of the film peaks indicated good crystallinity.

using Bragg's law and then using Vegard's law to calculate the concentration of TbAs in the film by linear interpolation (more details in Chapter 2).[36] The lattice constant of TbAs was obtained from an XRD spectrum taken of a 200 nm TbAs film grown on a GaAs substrate and capped with 50 nm of GaAs. This returned a value of 5.817Å which compares well with published values giving the lattice constant as 5.823Å.[37] We note that the sample preparation details (including degree of crystallinity) and source material purity of previously-measured TbAs materials were often not reported, making the accuracy of these measurements impossible to evaluate.[37] The concentrations of the two samples were found to be 6.6% TbAs (Tb source temperature 1320°C) and 10.4% TbAs (Tb source temperature 1345°C) by this method.

While this method initially seemed reasonable, recent data presented by Scarpulla et al. led us to believe that the thin film lattices may have been dilated by the nanoparticles more than expected by Vegard's law for a given concentration, as was found in ErAs:GaAs materials at concentrations greater than 1% (discussed in Chapter 2).[28] Following Scarpulla et al.'s methodology, Rutherford backscattering spectrometry was performed on the samples in order to reveal their true atomic concentrations.[28] It was found that a superdilation of lattice constant was occurring, and the actual concentrations of TbAs in the materials were 1.6±0.05% (1320°C) and 1.8±0.05% (1345°C). The exact cause of the superdilation is not well-known, but this phenomenon seems to occur at high levels of certain dopants in GaAs where doping is not purely substitutional, but where dopants may incorporate as precipitates, interstitials or complexes with lattice defects such as vacancies.[38] Additionally, thickness fringes visible in the XRD spectrum of the 1.6% TbAs sample allowed for

the calculation of the actual film thickness (~0.91μm). Film thicknesses were also calculated from RBS measurements and were in good agreement with XRD results. From RBS, the thickness of the 1.6% sample was found to be 1.00μm, and that of the 1.8% sample was found to be 1.06 μm. Finally, the narrow film peaks (FWHM were 0.005° and 0.009° for the 1.6% and 1.8% samples, respectively) and thickness fringes visible indicate that the films grown were uniform and of good crystalline quality.

3.1.2 Electrical and Thermal Properties

No values resulted from resistivity measurements as the resistance of both of the samples was too high to measure with the equipment (>$2x10^8\Omega$). This is consistent with predictions of a deeply-pinned Fermi level in TbAs:GaAs, as described in the introduction, where Shockley-Hall-Reed recombination limits electron conduction severely. Hall effect measurements were not possible either in the case of such resistive samples.

The thermal conductivities of both samples were successfully measured by TDTR. The room temperature thermal conductivity of the 1.6% TbAs sample was 17.6±1.8 W/m-K while that of the 1.8% sample was 10.8±1.8 W/m-K. Compared to the room temperature thermal conductivity measurement of a control sample of intrinsic GaAs, (50 W/m-K, which is in reasonable agreement with published values),[39] the presence of TbAs nanoparticles in the 1.8% TbAs sample was able to reduce the thermal conductivity by around five-fold. This is quite a significant reduction and a promising result for thermoelectric materials grown in a similar manner. Furthermore, since electrical conductivity was found to be so low in these materials, the electronic contribution to the thermal conductivity is almost zero (Wiedemann-Franz law - see Chapter 1).[1] The thermal conductance of the materials is

therefore due almost entirely to phonons and the reduction in thermal conductivity can be directly attributed to the nanoparticles.

Finally, PL measurements were performed on the 1.8% TbAs sample (Figure 3.2). PL quenching by about 75% was observed in comparison to a GaAs control sample (the back of the wafer), indicating that non-radiative recombination of photo-generated carriers was dominant. This signifies the existence of deep states, consistent with Fermi level predictions made in the introduction, as well as metallic behavior of the nanoparticles (non-radiative recombination).

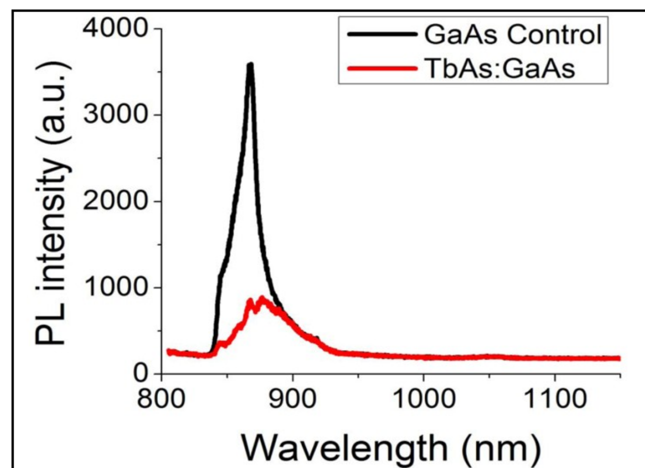

Figure 3.2: The photoluminescence signal from the 1.8% TbAs:GaAs film is quenched as seen by comparison to an undoped GaAs control spectrum (plot courtesy of Chelsea Haughn).

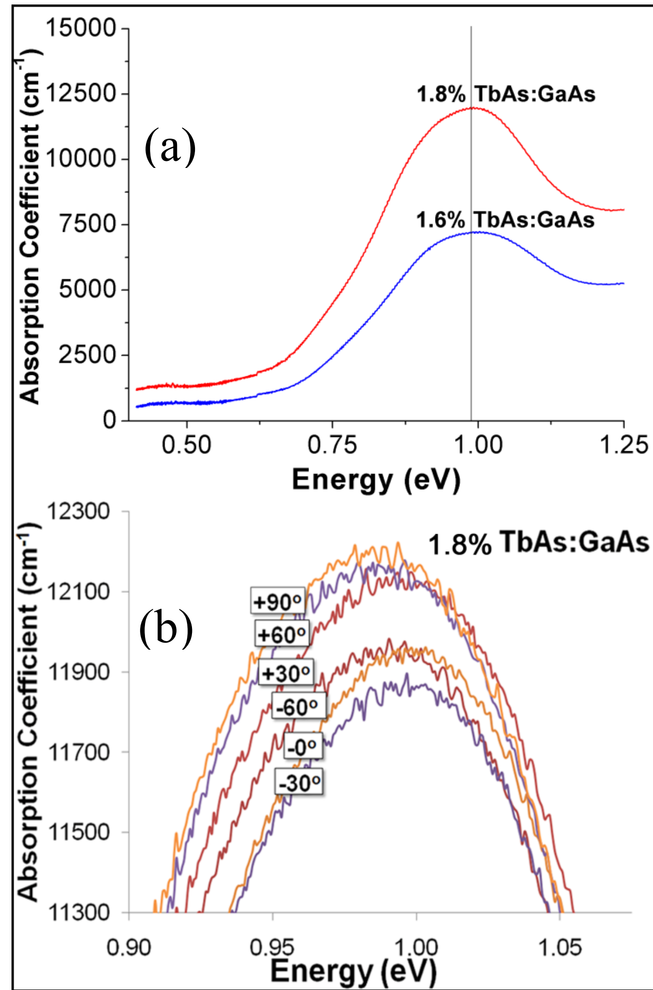

Figure 3.3: a) Optical absorption spectra from 1.6% and 1.8% TbAs:GaAs samples showing possible plasmon resonance peaks near 1 eV and indicating nanoparticle formation. b) The same peak is invariable under different light polarizations for the 1.8% TbAs sample, signifying possible isotropy of nanoparticle shape and distribution (plots courtesy of Peter Burke).

3.1.3 Nanoparticle Observation and Characterization

The presence of nanoparticles in TbAs:GaAs was suggested by OAS and confirmed by HAADF STEM. Both samples were first characterized with OAS (spectra are shown in figure 3.3a). In each case, an absorption peak was found at about 1 eV; this similarity to absorption spectra from InGaAs with ErAs nanoparticles strongly suggests the presence of TbAs nanoparticles within the material.[27] The origin of these sub-band gap peaks is unknown, but it is probable that the absorption is by plasmons at the surface of the nanoparticles. They could also correspond to a TbAs band gap if the strain on the nanoparticles was great enough to energetically shift the semimetal to a semiconductor. The fact that the peaks are at the same position for both concentrations suggests that the particles have similar carrier concentrations. Upon varying the angle of light polarization (Figure 3.3b), the peak intensities and positions for both samples did not differ appreciably, suggesting possible isotropy of nanoparticle shape and distribution.

To confirm the optical absorption measurements and the existence of nanoparticles, HAADF STEM was performed on the 1.8% TbAs:GaAs sample as shown in the plan-view images in Figure 3.4. Randomly-distributed particles of approximately uniform size are observed. From these images, an average particle diameter of ~1.5 nm was measured. The TbAs nanoparticles exhibit the bulk TbAs rock salt structure with a continuous As sublattice between the nanoparticles and the surrounding GaAs matrix. While further examination is needed, it appears that some of the nanoparticles were very slightly elongated in one of the <110> directions, which corresponds to the fast diffusion direction on a (001) GaAs growth surface. The average diameter of these nanoparticles was smaller than that of ErAs nanoparticles in GaAs referenced by Scarpulla et al. (2-3nm)[27] but similar to those grown by Singer et

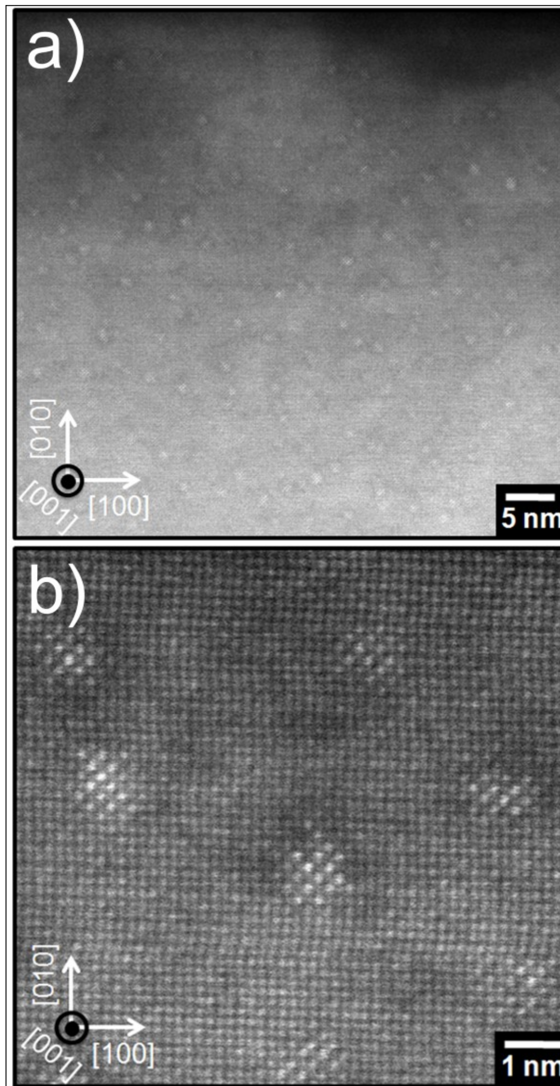

Figure 3.4: a) HAADF STEM plan-view images of self-assembled TbAs nanoparticles in GaAs grown on (001) GaAs and viewed along the $[00\bar{1}]$ direction with an approximate layer TbAs concentration of 1.8%. The average particle diameter was approximately 1.5 nm. b) The rock salt crystal structure of TbAs and continuous As sublattice throughout the sample are visible. TbAs appears bright in the images (images courtesy of Trevor Buehl).

al.[25] and Poole et al.[26] (1-2nm). This can be attributed at least partially to a lower growth temperature (490°C for this work vs. 580°C for most ErAs:GaAs growths), but other differences between terbium and erbium could also contribute to these differences.

3.2 Summary

Two samples of GaAs co-deposited with 1.6% and 1.8% TbAs concentrations were grown by MBE, and their electrical, thermal, and structural properties were explored. Formation of TbAs nanoparticles was confirmed through optical absorption and HAADF STEM. Moreover, high electrical resistivity and a lack of PL signal were consistent with energy band predictions and previous results in other rare earth-V/III-V nanocomposite systems.[6,7,9,10,27,40] Thermal conductivity was reduced significantly from that of the semiconductor matrix due to phonon scattering by the nanoparticles. Based on these analyses, we believe that co-depositing Tb in other III-V semiconductors, particularly InGaAs, will lead to efficiency improvements in thermoelectric materials. Additionally, TbAs-containing materials with short carrier lifetimes may be useful for photoconductive switches and other terahertz applications.

Chapter 4

TbAs:InGaAs NANOCOMPOSITES: RESULTS AND DISCUSSION

A series of samples consisting of $In_{0.53}Ga_{0.47}As$ (lattice-matched to InP) with epitaxially-embedded TbAs nanoparticles was fabricated and characterized for this project. These samples were grown by molecular beam epitaxy for the experimental purpose of designing a new n-type material which exhibits increased efficiency in thermoelectric power generation. The motivation for exploring this particular materials system is given in Chapter 1 while the growth and characterization methodology and details are given in Chapter 2. To reiterate, twenty TbAs:InGaAs samples were grown with TbAs atomic concentrations which varied from 0.06% to 14%. For control purposes, several pure InGaAs samples were also grown.

The physical structure of the samples was observed through high-angle annular dark field scanning electron microscopy (HAADF STEM) and x-ray diffraction (XRD). The thermoelectric properties were collected for the samples both at room temperature and over a wide temperature range with resistivity/Hall effect measurements, Seebeck coefficient measurements, and thermal conductivity measurements. Time-domain thermoreflectance (TDTR) was used to assess thermal conductivity at room temperature while this value was gathered from a few samples over a wide temperature range by the 3ω method. Thermoelectric power factor and figure of merit, ZT, are calculated where possible, and the performance of these materials is evaluated in comparison with similar well-performing nanocomposites.

4.1 Room Temperature Properties of TbAs:InGaAs Nanocomposites

4.1.1 Structure and Composition

Three samples of differing TbAs concentration (0.2%, 0.8%, and 14%) were examined with plan-view HAADF STEM. The 0.8% TbAs:InGaAs sample is shown in Figure 4.1a where randomly-dispersed nanoparticles can be seen which are more cubic than spherical in shape and have diameters of approximately 1nm. This size is slightly smaller than the nanoparticles of approximately 1.5nm diameter which were observed in 1.8% TbAs:GaAs and much smaller than those observed in some ErAs:GaAs growths (2-3nm).[27,29] Previous studies on the growth conditions of similar ErAs nanocomposites have revealed that the size of the nanoparticles does not seem to be dependent on the total rare earth concentration, but is more likely to be a function of growth temperature.[24,27] Nonetheless, these samples were grown with the same substrate growth temperature as the TbAs:GaAs samples, so a possible concentration dependence for TbAs nanoparticle size is noted. On the other hand, nanoparticles were not visible in the 0.2% TbAs sample micrograph. Conversely, nanoparticles were observed in 0.2% ErAs:InGaAs; this raises the possibility that Tb is more soluble in InGaAs than is Er (at the same growth temperature). If more single Tb atoms are dissolved in the InGaAs matrix for any given concentration, perhaps the remaining atoms would be few enough to form smaller nanoparticles, as in the 0.8% TbAs sample. However, if less available Tb resulted in smaller nanoparticles rather than fewer nanoparticles of the same size, then rare earth concentration would be expected to affect nanoparticle size as well. Little is known about TbAs growth conditions thus far, so it is certainly possible that there are differences in growth patterns between TbAs and ErAs. A micrograph of the 14% TbAs:InGaAs sample is shown in Figure

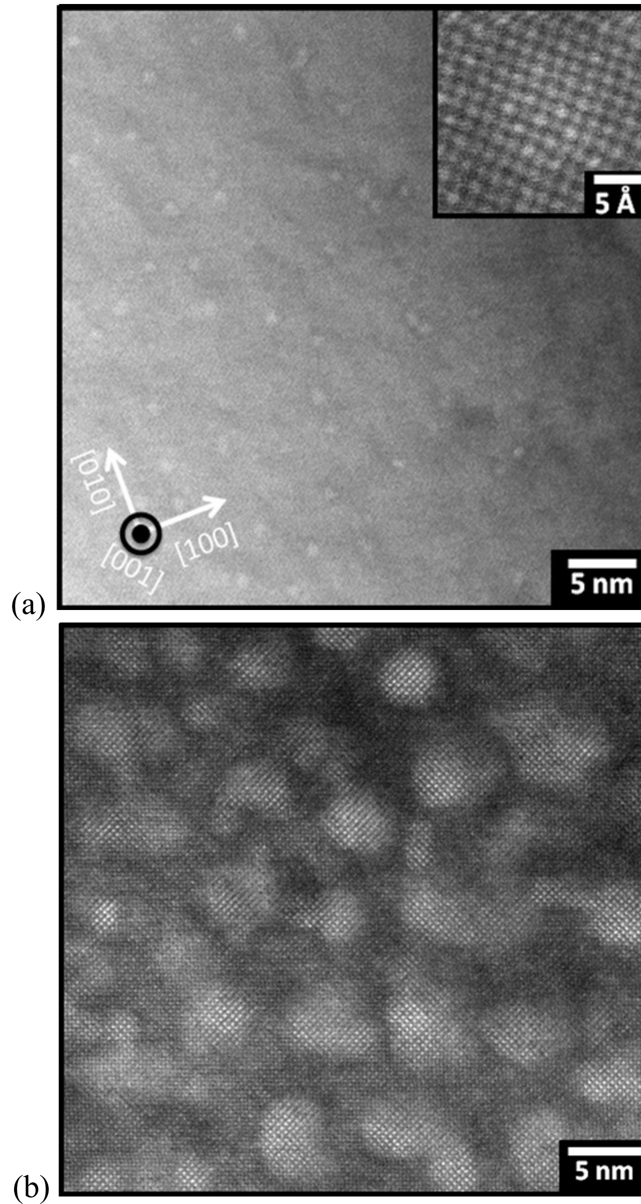

Figure 4.1: (a) Randomly-distributed TbAs nanoparticles of about 1nm in diameter were found using plan-view HAADF STEM on 0.8% TbAs:InGaAs. Nanoparticles appear similar but slightly smaller than those formed in TbAs:GaAs. (b) TbAs nanoparticles run together and lose uniformity in shape in a micrograph of 14% TbAs:InGaAs (images courtesy of Trevor Buehl).

4.1b. At this very high concentration, TbAs nanoparticles overlap in the image, making it difficult to discern whether nanoparticles are much bigger or just run together because of the high number of them. Nanoparticles no longer seem to be cubical or spherical in shape either. One might surmise that this vastly different structure might bring about dissimilar electrical and thermal properties as well. Lastly, as in TbAs:GaAs, the rocksalt crystal structure of TbAs and the continuous As sublattice throughout the samples are seen in these micrographs.

XRD spectra were collected for all of the TbAs:InGaAs samples. However, not much information was able to be gathered from these. For typical single crystal films, one would expect to see a peak for the substrate material, a peak for the active layer, and peaks from any buffer layers grown in between. In the case of these samples, some had a buffer layer and active layer (three peaks) whereas the rest were only the active layer on the substrate (two peaks). Each of the samples was found to have more than three peaks, however, so it was unclear which peaks were attributable to what material. The cause for this is unknown, but it does indicate that there are multiple lattice constants present in the thin film, representing possible phase segregation or graded InGaAs composition due to the unstable indium effusion cell. Thickness fringes were only observed for one sample. Therefore, it was impossible to use XRD to determine composition or layer thickness (for all but one sample).

4.1.2 Electrical Characterization

Room temperature resistivity and Hall Effect measurements were taken of each sample using van der Pauw geometry. Electrical conductivity, mobility, and electron carrier concentration were calculated from the results and are plotted versus

TbAs concentration in Figure 4.2. Hall Effect data from two samples (0.06% and 0.47%) are not reported due to a strong anisotropy between the two orthogonal in-plane directions, yielding resistances in tens of Ohms in one direction and megaOhms in the other. The cause of this anisotropy in these two samples (grown on the same day) is unclear, but all other samples were measurable and isotropic at least to the same order of magnitude. All data presented in this section includes a data point for the control sample with 0% TbAs (undoped InGaAs). Additionally, Figures 4.2 and 4.3 include data points from an InGaAs control sample which was doped with Si to the same level as a 0.8% TbAs:InGaAs sample (2.5×10^{18} cm^{-3}). This reference sample was created to question if TbAs nanoparticles provide a significant advantage over conventional doping. As expected, mobility decreases as TbAs nanoparticle concentration increases, providing more scattering centers for electrons. It is unclear why carrier concentration peaks at around 1% TbAs, but three samples with concentrations near this point show that this result is repeatable. As a result, conductivity peaks at the same concentration. Similar trends and magnitudes of these quantities were observed in ErAs:InGaAs, but the peak conductivity occurred around 0.2% instead of 0.8%. Because data is only available up to ~2% ErAs concentration in these samples, it is unclear whether or not carrier concentration also exhibits a peak value. Even so, the fact that at room temperature these TbAs:InGaAs samples compare well to ErAs:InGaAs samples, which showed significant increase in thermoelectric conversion efficiency at high temperatures, is encouraging.

Seebeck coefficient of each sample was measured at room temperature with a two point voltage and temperature measurement at either end of a bar of sample material. Figure 4.2d shows that the Seebeck coefficient decreases as TbAs

concentration increases – an effect which was also observed in ErAs:InGaAs. Recalling that Seebeck coefficient is essentially a function of the moment of the energy-dependent differential conductivity of electrons about the Fermi level of the

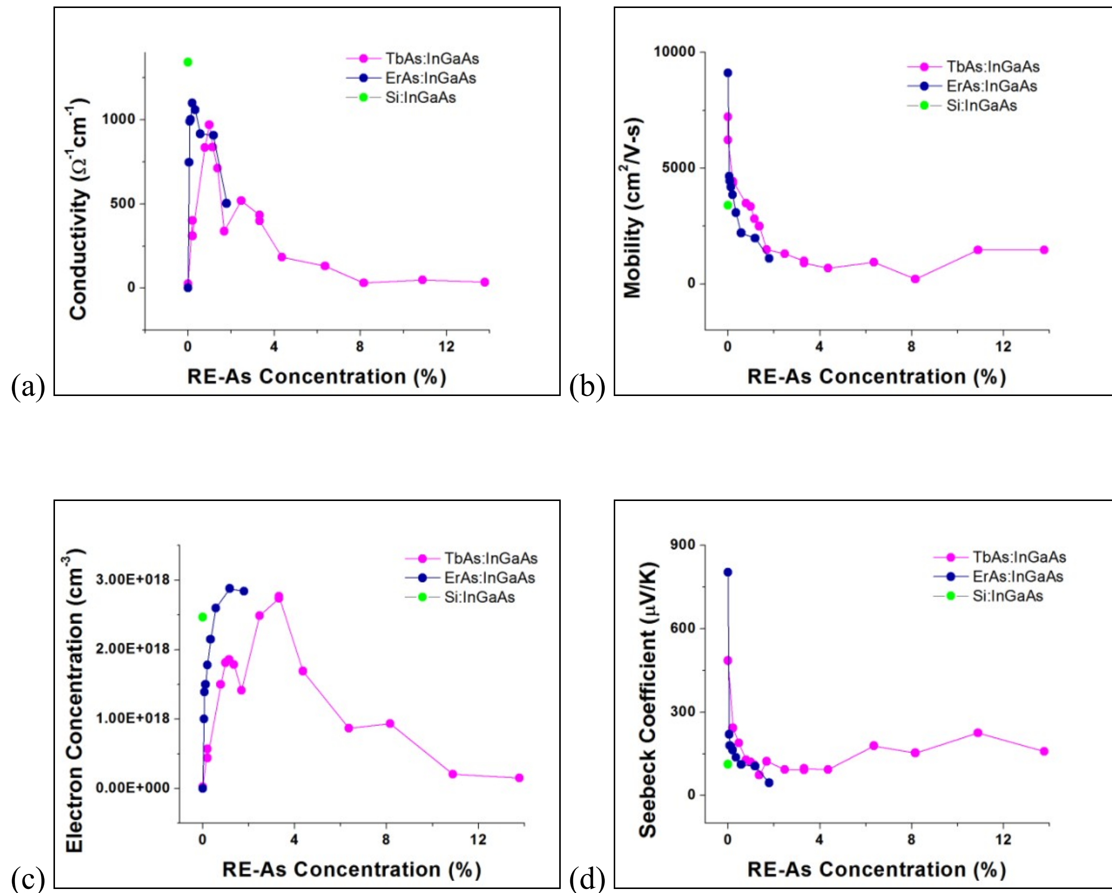

Figure 4.2: Room temperature electrical conductivity (a), electron mobility (b), electron carrier concentration (c) and Seebeck coefficient (d) of TbAs:InGaAs are plotted as a function of TbAs concentration. These values are compared with similar ErAs:InGaAs materials (ErAs data courtesy of Peter Burke, UCSB)[15].

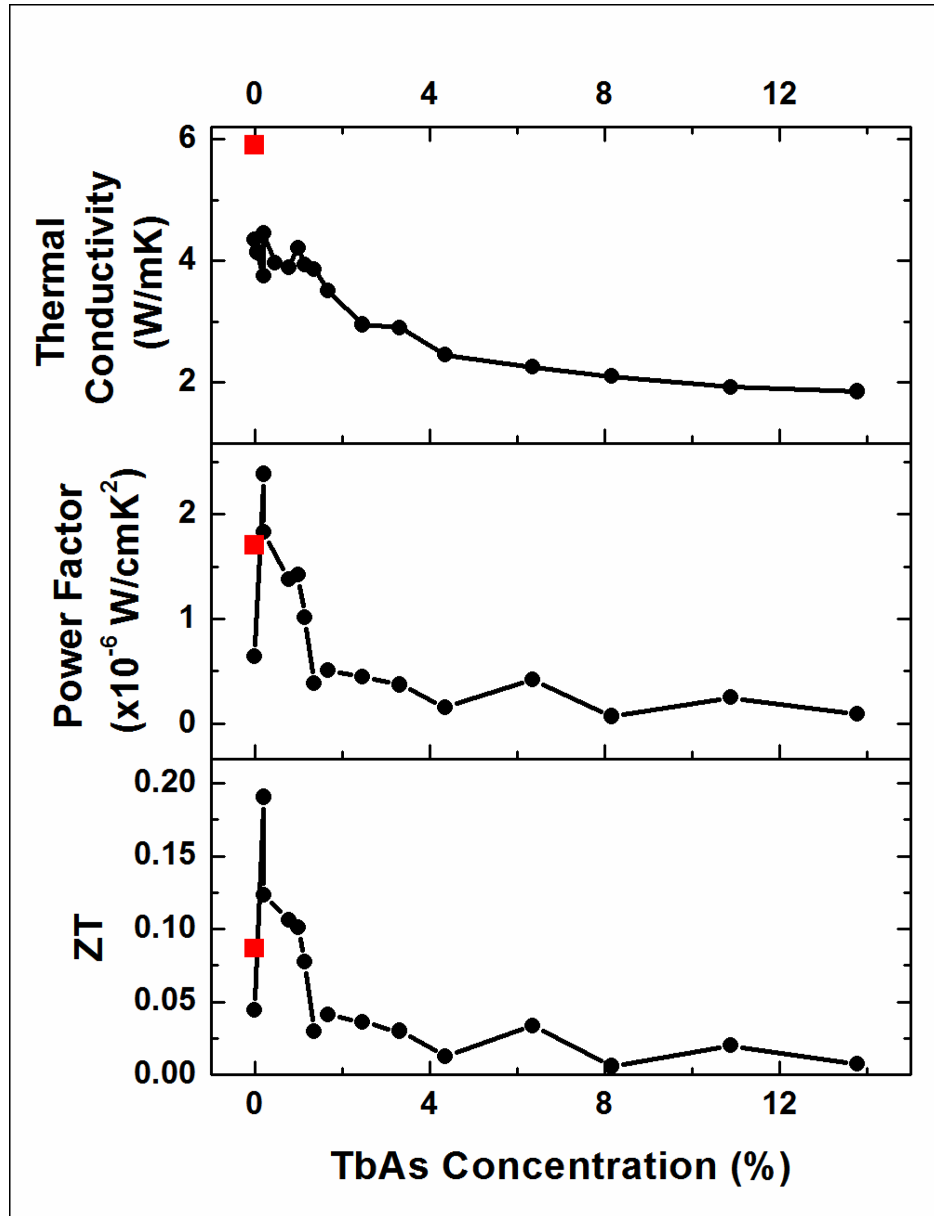

Figure 4.3: Room temperature thermal conductivity as measured by TDTR (a), thermoelectric power factor (b) and thermoelectric figure of merit, ZT (c), are plotted as a function of TbAs atomic concentration. A TbAs concentration which optimizes room temperature thermoelectric conversion efficiency is found to occur around 0.3%.

material, this result is expected;[41] as carrier concentration, and therefore electrical conductivity, increase with electron donation from nanoparticles, the degenerate Fermi level moves up in the parabolic conduction band, and the electron conductivities become more symmetric, decreasing this moment and the Seebeck coefficient. Similarly, when carrier concentration falls after its peak around 1% TbAs, Seebeck coefficient recovers somewhat for concentrations higher than this.

4.1.3 Thermal Characterization

Room temperature thermal conductivity data was gathered using TDTR (described in Chapter 2). Figure 4.3a shows that thermal conductivity decreases as more nanoparticles are introduced into the sample with the exception of the first few data points which stay around 3.5-4.5 W/mK. The presence of nanoparticles was expected to lower thermal conductivity significantly, mostly through phonon scattering. For concentrations greater than about 1.7%, thermal conductivity is reduced significantly from that of InGaAs (~5.5W/mK), just as TbAs nanoparticles greatly reduced the thermal conductivity of GaAs.[29] HAADF STEM results discussed earlier revealing the absence of nanoparticle formation at 0.2% TbAs could explain why thermal conductivity was not reduced much below that of pure InGaAs. Indeed, at low concentrations, Tb is merely acting as a conventional dopant.

4.1.4 Thermoelectric Performance

The thermoelectric power factor ($S^2\sigma$) which encompasses the electrical properties of the thermoelectric figure of merit, ZT ($S^2\sigma T/\kappa$), was calculated for each sample and is shown in Figure 4.3b. Room temperature ZT is shown in Figure 4.3c. Given the decreasing Seebeck coefficient with increasing TbAs concentration and

peaking conductivity around 1% TbAs, an ideal concentration is found for room temperature power factor and ZT, both of which occur at around 0.3%. This does not indicate that this concentration will perform best for high temperature applications. In fact, while similar ErAs:InGaAs materials peaked in power factor and ZT at around 0.05% at room temperature, an ErAs concentration of around 0.2% was found to be optimal for high temperatures.[15] The values of the maximum room temperature power factor and ZT are comparable to those of ErAs:InGaAs, although a few ErAs:InGaAs samples with 0.1%-0.2% ErAs concentrations exhibited a room temperature power factor slightly higher than any TbAs sample grown;[15] however, no TbAs:InGaAs samples have been grown in this narrow range, so similar behavior cannot be ruled out.

4.2 High Temperature Thermoelectric Properties of TbAs:InGaAs

The same TbAs:InGaAs samples were processed for high temperature measurement of electrical conductivity, mobility, and carrier concentration; Seebeck coefficient; and thermal conductivity. The process for preparing the samples for non-destructive high temperature measurement is described in Chapter 2. Given the complex processing procedure and long measurement times, not all twenty samples grown were able to be measured at high temperature.

4.2.1 Electrical Characterization

Resistivity and Hall Effect measurements were taken of eight TbAs:InGaAs samples with TbAs concentrations ranging from 0.2%-11% in a cryostat in 10 degree increments from 30-750K. Electrical conductivity, mobility, and carrier concentration were calculated from the results and are plotted for a few samples in

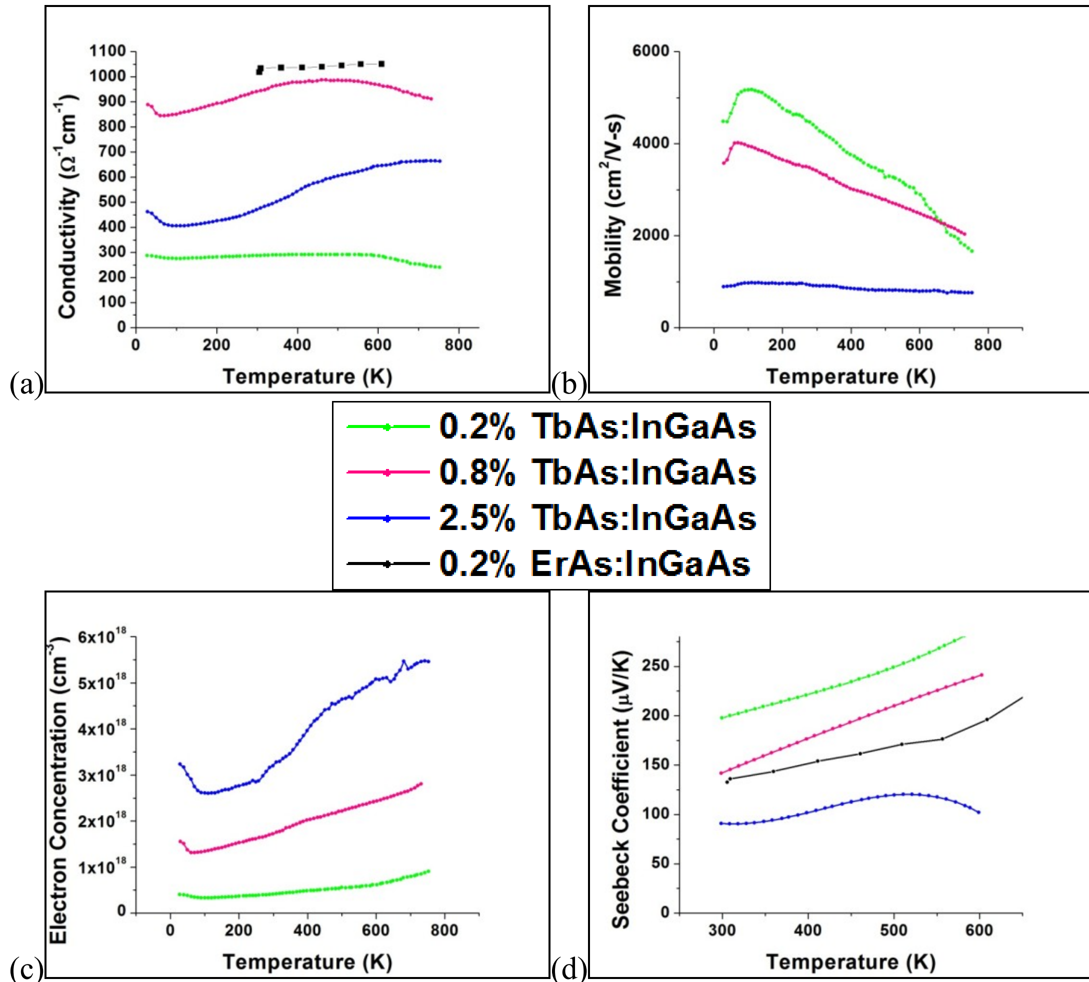

Figure 4.4: Electrical conductivity (a), mobility (b), and carrier concentration (c) of a few TbAs:InGaAs samples over a wide temperature range. The electrical conductivity of the ErAs:InGaAs sample which performed best for thermoelectrics (0.2% ErAs) is also shown. High temperature Seebeck coefficient (d) was measured as well and compared to the same 0.2% ErAs:InGaAs sample (ErAs data courtesy of Peter Burke, UCSB).[15]

Figure 4.4 (plotting all eight samples is a bit overwhelming). The electrical conductivity and Seebeck coefficient of these samples are also graphically compared with a 0.2% ErAs:InGaAs sample which was the best thermoelectric material found in that growth series. In general, data for each sample did not overlap with other samples, so it was clear which samples had the highest and lowest values over the whole temperature range. The TbAs:InGaAs sample which had the highest electrical conductivity over the entire temperature range contained 0.8% TbAs.

The high temperature Seebeck coefficient of seven of these samples was measured on one or both of two apparatuses (one located at UCSB, the other at UCSC). Unfortunately, there was some discrepancy between the two measurement systems which has yet to be resolved. Of the three samples plotted in Figure 4.4d, the 0.2% sample was measured at UCSC and the other two were measured at UCSB. The 0.8% sample was measured on both systems, and a plot comparing the two data sets is given in Figure 4.5. The trend is parallel up until around 600K, and before that point the data points are within about 20% of each other. After 600K, the InP substrate starts to conduct from thermally-excited intrinsic carriers, and the signal from the thin film is lost under this large amount of noise. It is unclear why the Seebeck coefficient gets very large above 600K on one system and very small above this point on the other system, but surely data after this turning point cannot be trusted from either system. Looking back to Figure 4.4d, it is clear that the lowest concentration samples exhibit the highest Seebeck coefficient, as was apparent from the room temperature data shown in Figure 4.2d. Calculating power factor will reveal which balance of electrical conductivity and Seebeck coefficient is best for thermoelectric performance.

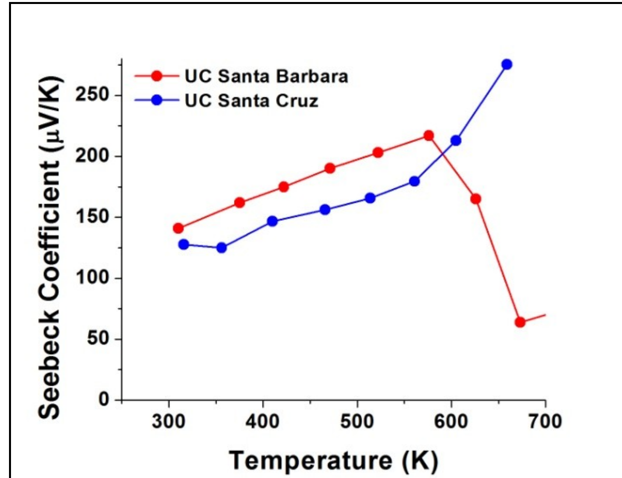

Figure 4.5: **Comparison of 0.8% TbAs:InGaAs high temperature Seebeck coefficient measurements from two different measurements systems utilized for this project. Data above ~600K is unreliable due to activated conduction from the InP substrate.**

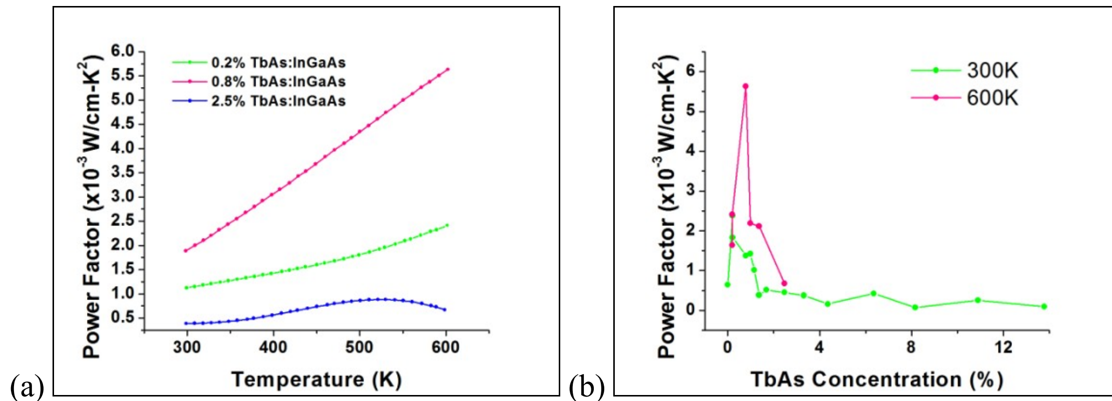

Figure 4.6: **Thermoelectric power factor calculation ($S^2\sigma$) for TbAs:InGaAs: (a) select samples of varying TbAs concentration over a wide temperature range; (b) power factor versus TbAs concentration at room temperature and at the highest temperature for reliable measurement (600K). The maximum power factor at 600K occurs at 0.8% TbAs while the maximum at room temperature occurs at 0.2% TbAs.**

It is again encouraging from a thermoelectric point of view that at least one of the TbAs:InGaAs samples compares very well with the best performing ErAs:InGaAs sample. As was described in the first chapter, the Fermi level of TbAs:InGaAs is expected to fall within the band gap of InGaAs, lower than that of ErAs:InGaAs which was measured to be slightly above the conduction band edge. If this were true, the electrical conductivity of TbAs:InGaAs would be expected to be slightly lower than that of ErAs:InGaAs and the Seebeck coefficient slightly higher than that of ErAs:InGaAs. This is indeed the case for these two samples of highest conductivity. Therefore, these data are consistent with the energy band predictions made in Chapter 1.

High temperature power factor was calculated for the seven samples for which both electrical conductivity and Seebeck coefficient data was available over the temperature range. Figure 4.6a shows this quantity for the same samples displayed in Figure 4.4 while Figure 4.6b shows that the concentration of TbAs possessing the best power factor is different at higher temperatures from what was found at room temperature. Indeed, the maximum power factor occurs at 0.8% TbAs at 600K whereas the highest power factor at room temperature occurred at 0.2% TbAs.

In Chapter 1, the proposed benefits of TbAs:InGaAs over ErAs-containing nanocomposites were discussed. The expected placement of the Fermi level of TbAs:InGaAs within the band gap of the semiconductor matrix is anticipated to increase power factor over ErAs materials by increasing Seebeck coefficient with a more appropriately-placed energy barrier. Figure 4.7 compares the 0.8% TbAs:InGaAs sample to the best performing ErAs materials – 0.2% ErAs:InGaAs and 0.6%

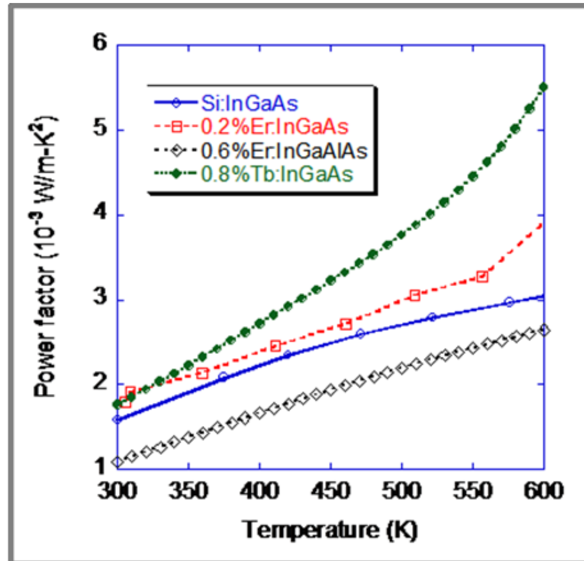

Figure 4.7: Power factor comparison of best-performing TbAs:InGaAs, ErAs:InGaAs, and ErAs:InGaAlAs materials with a Si-doped InGaAs control sample (figure courtesy of Dr. Zhixi Bian).

ErAs:InGaAlAs – along with an InGaAs control sample which was doped with Si at a level comparable to carrier concentration in the other contenders. The power factor of the 0.8% TbAs sample is indeed increased over all of these well-performing materials. This difference is quite significant at the highest temperatures; at 600K, the power factor of the TbAs:InGaAs sample, 5.63 mW/mK^2, is enhanced nearly 40% over the next highest sample. It also appears for all of the samples that power factor will continue to increase at temperatures greater than 600K. Since plenty of possible thermoelectric applications have heat sources which are higher in temperature than this, it is useful to know the thermoelectric properties above 600K. Therefore, efforts

are being made to remove the substrate of a couple of TbAs:InGaAs samples and a Si:InGaAs control sample, and data at even higher temperatures will be able to be collected in the near future.

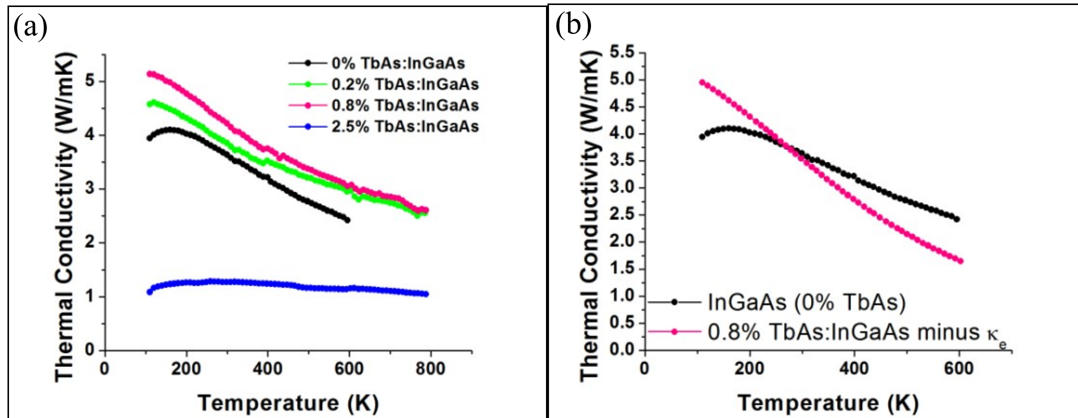

Figure 4.8: (a) Thermal conductivity data of TbAs:InGaAs and an undoped InGaAs sample, taken using the 3ω method. (b) Comparison of lattice component (electronic component subtracted) of 0.8% TbAs:InGaAs's thermal conductivity with the undoped InGaAs control sample.

4.2.2 Thermal Characterization

Thermal conductivity data from three TbAs:InGaAs samples was gathered from 100-800K using the 3ω method in a measurement system at UC Berkeley. Only these samples and an InGaAs thin film control sample were measured due to the labor-intensive processing procedure and the fact that only eleven of the twenty samples were even grown thick enough to measure accurately with this method. The thermal conductivity data of these four samples is plotted in Figure 4.8a. Interestingly, there is

an increase in thermal conductivity from that of pure InGaAs with the 0.2% and 0.8% samples. At 2.5%, however, there is a large reduction from InGaAs across the entire temperature range; the values are reduced by a minimum of 57% throughout the range.

Several suggestions can be made as to why the lower concentration samples exhibit higher thermal conductivities than pure InGaAs. First of all, it should be noted that the values measured for pure InGaAs do not match well with literature values which give a thermal conductivity of around 5.5 W/mK for $In_{0.53}Ga_{0.47}As$ at room temperature. In fact, this control sample's thermal conductivity was measured to be 3.64 W/mK at room temperature. This could be a measurement error, or this large discrepancy could be due to imperfect MBE growth conditions causing the exact composition of the compound to vary, perhaps even during growth. Another factor is that STEM images (described earlier) revealed that nanoparticles did not form in some of the lower concentration samples. One of the key goals of introducing nanoparticles into the material was to scatter phonons to lower thermal conductivity. If there were no nanoparticles, thermal conductivity would only be reduced by Tb impurity scattering, which would not provide any advantages over conventional Si doping. In the case of the 0.8% sample, there are indeed nanoparticles, but perhaps since they are smaller in size (and therefore scattering cross section) than similar ErAs materials and TbAs:GaAs nanoparticles, they scatter fewer phonons. Furthermore, the high electrical conductivity measured in this sample could cause the electronic contribution to the thermal conductivity to be significant, increasing the thermal conductivity far beyond resistive InGaAs. To test this, the electronic contribution was calculated using the Wiedemann-Franz Law and subtracted from the thermal conductivity values of 0.8% TbAs:InGaAs; this reduced thermal conductivity is plotted with that of the 0% sample

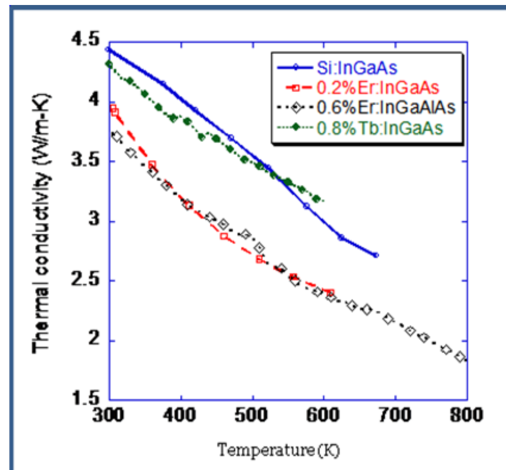

Figure 4.9: Comparison of 3ω thermal conductivity data of best-performing TbAs:InGaAs, ErAs:InGaAs, and ErAs:InGaAlAs materials with a Si-doped InGaAs control sample. Tb does not reduce the thermal conductivity of InGaAs any more than conventional Si doping (figure courtesy of Dr. Zhixi Bian).

in Figure 4.8b. With this adjustment, the numerical values much more closely match those of this InGaAs sample, but the downward slope with increasing temperature is steeper on the 0.8% TbAs sample, causing the two lines to cross around 270K. Perhaps the most important thing to note, however, is that with only 0.2% ErAs nanoparticles in InGaAs, thermal conductivity was reduced significantly from a control sample (Si:InGaAs, not the same 0% sample), even though electrical conductivity was higher in this sample than the 0.8% TbAs sample (Figure 4.9). This figure also shows that the thermal conductivity of Si doping in InGaAs is nearly the same as 0.8% TbAs:InGaAs. Clearly, ErAs nanoparticles effectively scatter phonons while TbAs nanoparticles do not. This leads us to believe that it is not the mass of the

nanoparticles that is causing phonon scattering, but the strain field around the nanoparticle. TbAs is much less strained (0.9% tensile mismatch) than ErAs (2.2% tensile mismatch) in InGaAs, so perhaps the increased strain with ErAs nanoparticles brings about energetic barriers around the nanoparticles that scatter phonons more effectively.

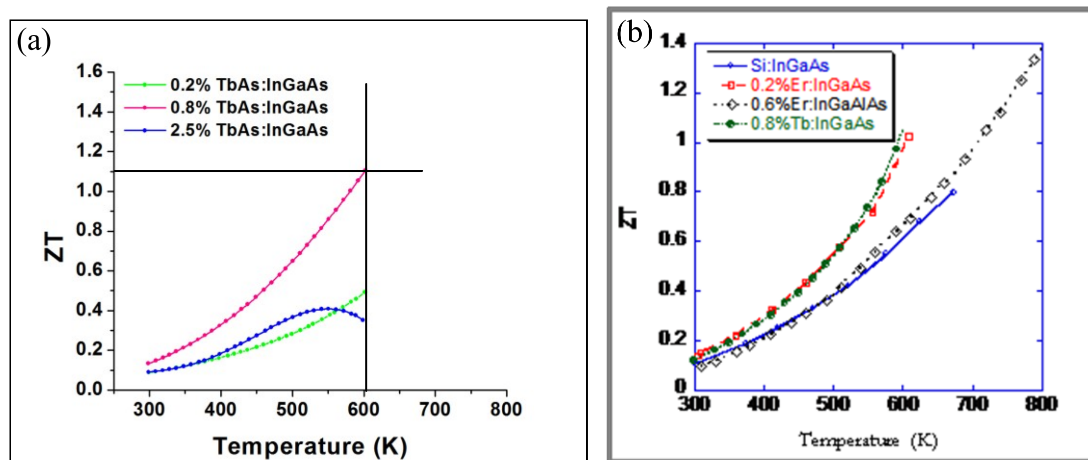

Figure 4.10: Thermoelectric figure of merit, ZT, as a function of testing temperature for (a) TbAs:InGaAs with varying TbAs concentrations and (b) in comparison with the same well-performing ErAs samples and Si:InGaAs control sample (plot (b) courtesy of Dr. Zhixi Bian).

Finally, the power factor and thermal conductivity data presented above were combined to calculate the figure of merit, ZT, for the TbAs:InGaAs materials and evaluate their potential for thermoelectric applications. ZT of the three TbAs:InGaAs

samples for which both power factor and thermal conductivity data were available is plotted in Figure 4.10a. The highest ZT (1.1 at 600K) is found in the 0.8% TbAs sample. Although data could only be collected up to 600K at this time, it is clear from this plot that at higher temperatures the ZT of this material will continue to increase. Visually extrapolating, one might even expect ZT of 1.5 or 2 at 800K, which would be very useful for high temperature thermoelectric applications, particularly because the material efficiency is also a function of the Carnot efficiency which is greater at higher temperature differences. Comparing ZT to the same ErAs and Si:InGaAs samples as above, 0.8% TbAs:InGaAs performs quite similarly to 0.2% ErAs:InGaAs, and both are more efficient than the other two samples (Figure 4.10b). Though these two samples come out with about the same efficiency, the TbAs sample's efficiency increase over Si:InGaAs is due entirely to power factor enhancement while the increase in ErAs:InGaAs is due mostly to thermal conductivity reduction. ErAs nanoparticles seem to scatter phonons better while TbAs nanoparticles increase power factor better.

4.3 Summary

The results from a series of TbAs:InGaAs nanocomposite growths with varying TbAs concentrations were presented and discussed. Room temperature electrical and thermal transport properties were measured, and plan-view HAADF STEM images were taken to observe the physical structure of the samples. Most of the results strongly paralleled those found in ErAs:InGaAs, a thermoelectric material which performed well at high temperatures, leading us to expect similarly promising results from TbAs:InGaAs at high temperatures. A significant difference found between ErAs and TbAs materials was a lack of nanoparticle formation in TbAs

materials at low concentrations where nanoparticles were found in ErAs composites. Samples were then processed for high temperature measurement and characterized electrically and thermally over from 300 to 600K. In both cases, thermoelectric power factor and ZT were calculated, and the TbAs concentrations which exhibited optimal thermoelectric performance were noted. At room temperature, 0.2% TbAs nanoparticles in InGaAs yields the highest power factor and ZT while at 600K (and likely above), 0.8% TbAs yields the highest power factor and ZT.

Chapter 5

CONCLUSIONS AND FUTURE WORK

In this project, the growth and characterization of TbAs/III-V semiconductor nanocomposites were explored for the purpose of improving efficiency for thermoelectric power generation applications. The growth of these novel materials was motivated by theory which predicted an improved thermoelectric power factor over similar ErAs nanocomposites, leading to higher thermoelectric conversion efficiency. This enhancement in power factor was expected to occur primarily due to improvement in Seebeck coefficient, but the high electrical conductivity and low thermal conductivity observed in similar nanocomposites were expected to characterize these TbAs-containing materials as well.

Two major series of material growths were completed by molecular beam epitaxy. Each thin film sample grown was characterized by several different techniques for structural, electrical, and thermal properties. TbAs:GaAs nanocomposites were grown to reveal the effect of TbAs nanoparticles on the properties of GaAs in comparison with an energy band model prediction as well as to observe the formation and physical characteristics of the nanoparticles. The results were found to be consistent with the energy band model, and HAADF STEM revealed random TbAs nanoparticles which were fully incorporated into GaAs matrix. The nanoparticles served to reduce thermal conductivity by about five-fold at an atomic concentration of 1.8% TbAs.

In the next growth series, InGaAs lattice matched to InP was grown with varying concentrations of randomly-distributed TbAs nanoparticles. HAADF STEM of a 0.8% TbAs:InGaAs sample revealed the formation of nanoparticles of slightly smaller diameter than in GaAs, but no nanoparticles were found in a 0.2% TbAs sample. The electrical and thermal transport properties of the materials were measured at room temperature and over a wide temperature range, up to 600K. At room temperature, a 0.2% TbAs sample exhibited the highest thermoelectric power factor and figure of merit, ZT. At higher temperatures, however, a 0.8% TbAs:InGaAs sample demonstrated the highest power factor and ZT, and therefore would be the most efficient material grown for thermoelectric applications. At 600K, this sample reached a ZT of 1.1 and will likely exhibit an even higher ZT at higher temperatures when this is made possible by substrate removal. This best TbAs:InGaAs sample compared well with similar well-performing ErAs:InGaAs samples at room temperature. It was noted in higher temperature measurements, however, that the TbAs material exhibited a slightly higher Seebeck coefficient and slightly lower electrical conductivity than the comparable ErAs sample, demonstrating consistency with the energy band model proposed. These differences constituted a much higher power factor than the best ErAs:InGaAs and ErAs:InGaAlAs samples, but TbAs:InGaAs's thermal conductivity was not reduced at all from control samples whereas ErAs nanoparticles served to significantly reduce this quantity. It is hypothesized that this lack of thermal conductivity reduction stems from a much smaller strain field around TbAs nanoparticles in InGaAs than is brought about by ErAs nanoparticles. In the end, the temperature-dependent ZT of 0.8% TbAs:InGaAs was nearly identical to the best ErAs:InGaAs sample and much higher than the best ErAs:InGaAlAs sample. The

improved ZT of the TbAs material was due fully to power factor increase while the high ZT of the ErAs:InGaAs material was due mostly to reduction of thermal conductivity. A logical solution to improve thermoelectric conversion efficiency even further, then, is to attempt to take advantage of both the power factor improvement from TbAs nanoparticles and the thermal conductivity reduction from ErAs nanoparticles. The next progression in this project, which has already been begun, will be to co-deposit both Er and Tb rare earth metals with InGaAs. The structure of the nanoparticles is as of yet unknown (separate ErAs and TbAs nanoparticles, ErTbAs mixed nanoparticles, or a core/shell structure), but we hope to exploit the benefits of both Er and Tb for thermoelectric efficiency enhancement.

Other future work will include optimization of a TbErAs:InGaAs material system as well as exploration of the effects on thermoelectric performance of conventional doping (most likely by silicon), of alloying the matrix with aluminum and/or bismuth, and of varying the composition of InGaAs away from lattice-matching to InP. Furthermore, varying growth conditions such as substrate temperature, growth rate, and sample thickness will assist in understanding the fundamentals of these nanocomposites better and will help optimize nanoparticle size for thermoelectric efficiency purposes. As high-quality thermoelectric materials are engineered and grown, effort will be made to make higher temperature measurements by removing the substrate of such samples. Furthermore, thermoelectric devices may be made with these materials in the future, and efficiency may be directly measured. On the characterization side of this project, efforts will be made to explore and dissolve discrepancies between measurement systems and methods. For example, there are small discrepancies between the two high temperature Seebeck coefficient

measurement systems used (UCSB, UCSC – discussed in Chapter 4) and between the TDTR and 3ω methods used for thermal conductivity measurement. Lastly, endeavors are currently being and will continue to be made to lower the cost of producing these nanocomposites. It is no secret that MBE is a very expensive and inefficient technique for material synthesis (albeit very valuable for materials research), but the only other current method that can parallel its accuracy and cleanliness is metal-organic chemical vapor deposition (MOCVD). Thus, experiments are ongoing to attempt to grow the same materials (ErAs and ErSb materials for the time being) with this cheaper and more efficient method. Bulk growth of these materials is also possible, but efforts made thus far have been difficult and resulted in poor-quality materials.

REFERENCES

[1] D. M. Rowe, ed., *CRC Handbook of Thermoelectrics*. CRC Press (1995).

[2] J. M. O. Zide, "Molecular Beam Epitaxial Growth of III-V Semimetal/III-V Semiconductor Nanocomposites for Energy Conversion Applications," *PhD dissertation*, University of California, Santa Barbara (2007).

[3] C. J. Vineis, A. Shakouri, A. Majumdar, and M. G. Kanatzidis, "Nanostructured Thermoelectrics: Big Efficiency Gains from Small Features," *Advanced Matererials* **22**, 3970-0980 (2010).

[4] W. Kim, J. Zide, A. Gossard, D. Klenov, S. Stemmer, A. Shakouri, and A. Majumdar, "Thermal Conductivity Reduction and Thermoelectric Figure of Merit Increase by Embedding Nanoparticles in Crystalline Semiconductors," *Physical Review Letters* **96**, 045901 (2006).

[5] D. Vashaee and A. Shakouri, "Improved Thermoelectric Power Factor in Metal-Based Superlattices," *Physical Review Letters* **92**, 106103 (2004).

[6] M. Hanson, S. Bank, J. Zide, J. Zimmerman, and A. Gossard, "Controlling electronic properties of epitaxial nanocomposites of dissimilar materials," *Journal of Crystal Growth* **301-302**, 4 (2007).

[7] D. C. Driscoll, M. Hanson, C. Kadow, and A. C. Gossard, "Electronic structure and conduction in a metal-semiconductor digital composite: ErAs:InGaAs," *Applied Physics Letters* **78**, 1703 (2001).

[8] C. Kadow, S. B. Fleischer, J. P. Ibbetson, J. E. Bowers, and A. C. Gossard, "Self-assembled ErAs islands in GaAs: Growth and subpicosecond carrier dynamics," *Applied Physics Letters* **75**, 3548 (1999).

[9] D. G. Cahill, W. K. Ford, K. E. Goodson, G. D. Mahan, A. Majumdar, H. J. Maris, R. Merlin, and S. R. Phillpot, "Nanoscale thermal transport," *Journal of Applied Physics* **93**, 793 (2003).

[10] J. M. Zide, D. O. Klenov, S. Stemmer, A. C. Gossard, G. Zeng, J. E. Bowers, D. Vashaee, and A. Shakouri, "Thermoelectric power factor in semiconductors with buried epitaxial semimetallic nanoparticles," *Applied Physics Letters* **87**, 112102 (2005).

[11] P. Pohl, F. H. Renner, M. Eckardt, A. Schwanhausser, A. Friedrich, O. Yuksekdag, S. Malzer, G. H. Dohler, P. Kiesel, D. Driscoll M. Hanson, and A. C. Gossard, "Enhanced recombination tunneling in GaAs pn junctions containing low-temperature-grown-GaAs and ErAs layers," *Applied Physics Letters* **83**, 4035 (2003).

[12] Woochul Kim, Suzanne L. Singer, Arun Majumdar, Joshua M. O. Zide, Dmitri Klenov, Arthur C. Gossard, and Susanne Stemmer, "Reducing Thermal Conductivity of Crystalline Solids at High Temperature Using Embedded Nanostructures," *Nano Letters* **8**, 2097 (2008).

[13] Peter G. Burke, Hong Lu, Nicholas G. Rudawski, Susanne Stemmer, Arthur C. Gossard, Je-Hyeong Bahk, and John E. Bowers, "Electrical properties of Er-doped $In_{0.53}Ga_{0.47}As$," *Journal of Vacuum Science and Technology B* **29**, 03C117 (2011).

[14] J. M. O. Zide, J.-H. Bahk, R. Singh, M. Zebarjadi, G. Zeng, H. Lu, J. P. Feser, D. Xu, S. L. Singer, Z. X. Bian, A. Majumdar, J. E. Bowers, A. Shakouri, and A. C. Gossard, "High efficiency semimetal/semiconductor nanocomposite thermoelectric materials," *Journal of Applied Physics* **108**, 123702 (2010).

[15] Peter Burke, University of California, Santa Barbara, *personal communication* (July 2011, unpublished data).

[16] Chun-gang Duan, R. F. Sabiryanov, W. N. Mei, P. A. Dowben, S. S. Jaswal, E. Y. Tsymbal, "Electronic, magnetic and transport properties of rare-earth monopnictides," *Journal of Physics: Condensed Matter* **19**, 315220 (2007).

[17] K. Delaney, N. Spaldin, and C. Van de Walle, "Theoretical study of the structural and electronic properties of strained ErAs," *Physical Review B* **77**, 235117 (2008).

[18] L. H. Brixner, "Structure and electrical properties of some new rare earth arsenides, antimonides and tellurides," *Journal of Inorganic and Nuclear Chemistry* **15**, 199 (1960).

[19] F. Hulliger, *Handbook on the Physics and Chemistry of Rare Earths*, ed. K.A. Gschneidner and L. Eyring, Vol. 4, North Holland (1979).

[20] K. Delaney, *personal communication* (April 2011).

[21] M. A. Herman and H. Sitter, *Molecular Beam Epitaxy: Fundamentals and Current Status*, 2nd ed., Springer (1996).

[22] Image from: "Stranski-Krastanov Growth," Wikipedia (2011). Available from: http://en.wikipedia.org/wiki/Stranski%E2%80%93Krastanov_growth (accessed Jun 2011). Public domain.

[23] Hong Lu, University of California, Santa Barbara, *personal communication* (February 2010).

[24] D. O. Klenov, J. M. O. Zide, J. M. LeBeau, A. C. Gossard, and S. Stemmer, "Ordering of ErAs nanoparticles embedded in epitaxial InGaAs layers," *Applied Physics Letters* **90**, 121917 (2007).

[25] K. E. Singer, P. Rutter, A. R. Peaker, and A. C. Wright, "Self-organizing growth of erbium arsenide quantum dots and wires in gallium arsenide by molecular beam epitaxy," *Applied Physics Letters* **64**, 707-709 (1994).

[26] I. Poole, K. E. Singer, A. R. Peaker, and A. C. Wright, "Growth and structural characterization of molecular beam epitaxial erbium-doped GaAs," *Journal of Crystal Growth* **121**, 121 (1992).

[27] M. A. Scarpulla, J. M. O. Zide, J. M. LeBeau, C. G. Van de Walle, A. C. Gossard, and K. T. Delaney, "Near-infrared absorption and semimetal-semiconductor transition in 2nm ErAs nanoparticles embedded in GaAs and AlAs," *Applied Physics Letters* **92**, 173116 (2008).

[28] M. A. Scarpulla, T. E. Buehl, B. Mellot, R. V. Chopdekar, K. M. Yu, R. Farshchi, and A. C. Gossard, Presentation, "Properties of MBE-grown layers of III-V arsenides with embedded ErAs nanoparticles," *North American Molecular Beam Epitaxy Conference*, Breckenridge, Colorado (2010).

[29] L. E. Cassels, T. E. Buehl, P. G. Burke, C. J. Palmstrøm, A. C. Gossard, G. Pernot, A. Shakouri, C. R. Haughn, M. F. Doty, and J. M.O. Zide, "Growth and Characterization of TbAs:GaAs Nanocomposites," *Journal of Vacuum Science and Technology B* **29**, 03C114 (2011).

[30] L. J. van der Pauw, "A method of measuring the resistivity and Hall coefficient on lamellae of arbitrary shape," *Philips Technical Review* **20**, 220 (1958).

[31]National Institute of Standards and Technology, "The Hall Effect," available from: http://www.nist.gov/pml/semiconductor/hall_effect.cfm#lorentz (accessed June 2011).

[32] D. G. Cahill, W. K. Ford, K. E. Goodson, G. D. Mahan, A. Majumdar, H. J. Maris, R. Merlin, and S. R. Phillpot, "Nanoscale Thermal Transport," *Journal of Applied Physics* **93**, 793 (2003).

[33] S. Dilhaire, J. M. Rampnoux, S. Grauby, G. Pernot, and G. Calbris, "Nanoscale Thermal Transport Studied With Heterodyne Picosecond Thermoreflectance," *Proceedings of the ASME Micro/Nanoscale Heat and Mass Transfer International Conference* (2009).

[34] D. G. Cahill, "Thermal-Conductivity Measurement from 30 to 750 K – the 3ω Method," *Review of Scientific Instruments* **61**, 802 (1990).

[35] D. G. Cahill, M. Katiyar, and J. R. Abelson, "Thermal-Conductivity of Si:H Thin-Films," *Physical Review B* **50**, 6077 (1994).

[36] A. R. Denton and N. W. Ashcroft, "Vegard's Law," *Physical Review A* **43**, 3161 (1991).

[37] K. A. Gschneidner, Jr. and F. W. Calderwood, "The As-Tb (Arsenic-Terbium) system," *Journal of Phase Equilibria* **7**, 351 (1986).

[38]J. B. Mullin, B. W. Straughan, C. M. H. Driscoll, and A. F. W. Willoughby, "Lattice superdilation phenomena in doped GaAs," *Journal of Applied Physics* **47**, 2584 (1976).

[39] P. D. Maycock, "Thermal conductivity of silicon, germanium, III–V compounds and III–V alloys," *Solid-State Electronics* **10**, 161 (1967).

[40] J. Zide, D. Vashaee, Z. Bian, G. Zeng, J. Bowers, A. Shakouri, and A. Gossard, "Demonstration of electron filtering to increase the Seebeck coefficient in $In_{0.53}Ga_{0.47}As/In_{0.53}Ga_{0.28}Al_{0.19}As$ superlattices," *Physical Review B* **74**, 205335 (2006).

[41]Z. Bian, M. Zebarjadi, R. Singh, Y. Ezzahri, A. Shakouri, G. Zeng, J.-H. Bahk, J. Bowers, J. Zide, and A. Gossard, "Cross-plane Seebeck coefficient and Lorenz number in superlattices," *Physical Review B* **76**, 205311 (2007).

Appendix

REPRINT PERMISSION LETTERS

Reprint Permission for Figures 1.1, 2.4a, and 2.5:

Laura Cassels <laura.cassels@gmail.com>

Permission to use figures

2 messages

Laura Cassels <laura.cassels@gmail.com> — **Tue, Jul 26, 2011 at 6:23 PM**
To: Joshua Zide <zide@udel.edu>

Hi Joshua,

Can you please confirm that I can use the following figures from your dissertation in my thesis? (this is official)

Thank you,
Laura

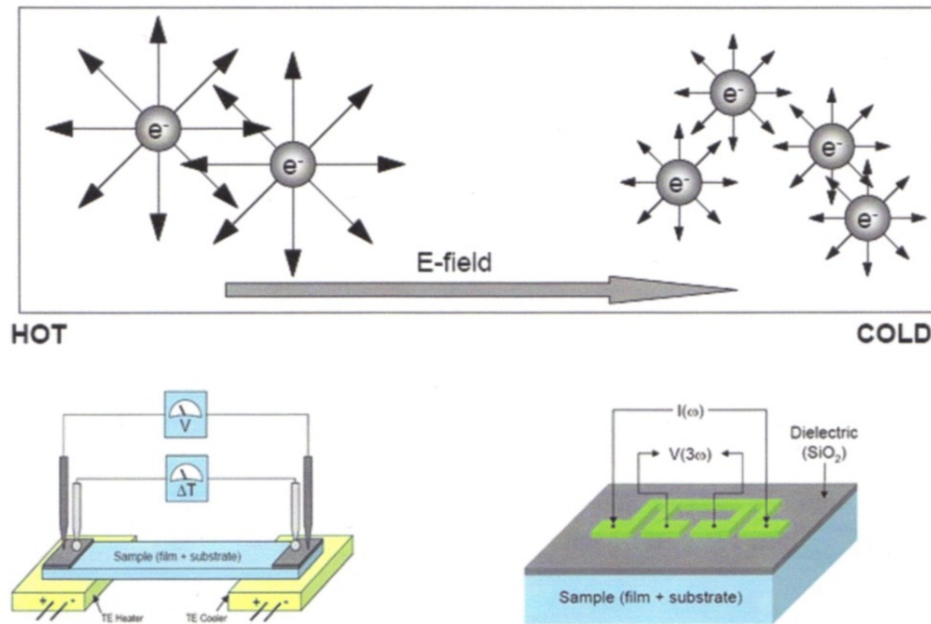

Joshua M. O. Zide <zide@udel.edu> — **Tue, Jul 26, 2011 at 6:38 PM**
To: Laura Cassels <laura.cassels@gmail.com>

You have my permission.

Best,
Joshua

Reprint Permission for Figure 1.4:

Laura Cassels <laura.cassels@gmail.com>

Use of figures for thesis

3 messages

Laura Cassels <laura.cassels@gmail.com> **Mon, Jul 4, 2011 at 3:03 PM**
To: Kris Delaney <kris.delaney@gmail.com>

Hi Kris,

I was just wondering if I may use a couple of your figures from your 2008 Phys. Rev. B paper in my thesis. I would like to use figures 1 and 4. Please let me know. Thank you very much!

Laura Cassels

Kris Delaney <kris.delaney@gmail.com> **Mon, Jul 4, 2011 at 4:56 PM**
To: Laura Cassels <laura.cassels@gmail.com>

Hi Laura,

That's totally fine with me. I think the convention is that copyright has been transferred to the publisher once the paper is accepted, so I don't think it's even my decision! But feel free anyway :)

Good luck!
Kris.

--
-=-
Kris Delaney

Materials Research Laboratory,
University of California,
Santa Barbara CA 93106-5121, USA

Email: kdelaney@mrl.ucsb.edu
Web: http://www.mrl.ucsb.edu/~kdelaney
Room: MRL 3113
-=-
[Quoted text hidden]

Laura Cassels <laura.cassels@gmail.com> **Mon, Jul 4, 2011 at 10:20 PM**
To: Kris Delaney <kris.delaney@gmail.com>

Hi Kris,

Actually, the APS website says the author may grant permission to reuse figures: http://publish.aps.org.proxy.nss.udel.edu/info/terms.html. So thank you very much!

Laura
[Quoted text hidden]